Experimental and numerical studies on mechanical properties of TPMS structures

Na Qiu[1], Yuheng Wan[1], Yijun Shen[2,*], Jianguang Fang[3,*]

[1] Mechanical and Electrical Engineering College, Hainan University, Haikou, 570228, China

[2] State Key Laboratory of Marine Resource Utilization in South China Sea, Hainan University, Haikou, 570228, China

[3]School of Civil and Environmental Engineering, University of Technology Sydney, Sydney, NSW 2007, Australia

ABSTRACT

Due to their exceptional lightweight and mechanical properties, triply periodic minimal surface (TPMS) based lattice structures have been widely studied. In this paper, the energy absorption performance of eight TPMS structures under large deformation was thoroughly studied, and five meshing strategies were evaluated comprehensively for the first time. The research objectives include three parts. First, the mechanical properties of eight TPMS structures, namely Primitive (P), Gyroid (G), Diamond (D), I-Wrapped Package (I-WP), Fischer-Kock (F-K), Neovius (N), I_2-Y** and F-Rhombic Dodecahedra (F-RD) lattices, were investigated by utilizing experimental and numerical methods. These TPMS structures were fabricated using 316L stainless steel powder by selective laser melting (SLM) and compared experimentally under compression in terms of the stress-strain curve, deformation and energy absorption. The results showed that F-RD and D lattice structures exhibit the best energy absorption capacity at relative densities less and greater than 30%, respectively. Second, to evaluate different meshing strategies for these complex structures, five finite elements (FE) models based on the shell, solid, and voxel elements were compared in terms of modeling ease, computational efficiency, data management, and simulation accuracy. It was demonstrated that the quadrilateral shell model shows satisfactory results for lattice structures with low relative densities or thin walls. In contrast, the voxel model shows the best results

Corresponding author: Yijun Shen: yshen2000@163.com
Corresponding author: Jianguang Fang: Jianguang.Fang@uts.edu.au

for structures with higher relative densities or thicker walls. Last, the voxel model was applied to the F-RD and D lattice structures. The numerical results showed that the stress distribution was more uniform in the F-RD, and the internal self-contact occurred later in the D lattice structure, further confirming the experimental observation and revealing the energy absorption mechanisms of TPMS structures.

Keywords: Triply periodic minimal surface, Selective laser melting, Finite elements, Energy absorption, Mechanical property

1. Introduction

Lattice structures have been studied extensively due to their outstanding physical, mechanical, thermal [1, 2], electrical [3], and acoustic properties [4]. They exhibit great potential for lightweight design and energy absorption [5, 6]. A novel class of lattice structures, the triply periodic minimum surface (TPMS) lattices, have aroused great interest due to their incredibly high strength and energy absorption [7, 8]. Compared to conventional lattice structures, the unique surface of TPMS structures results in an average curvature of zero [9, 10], which allows for a more uniform stress distribution that can carry more loads and produce smoother crushing [11]. However, it is challenging to produce TPMS lattice structures using traditional manufacturing techniques due to their complex geometries [12].

Additive manufacturing (AM) makes it possible to produce these complex TPMS structures [13]. As one of the most commercially utilized AM methods [14], selective laser melting (SLM) has successfully processed materials, including but not limited to steels, titanium alloys [15], aluminum alloys [16], and other metals [17, 18]. The development of SLM allows researchers to produce TPMS structures based on designed 3D models [19]. For example, Zhang et al. [20] used SLM to fabricate 15 G lattice structures with uniform and graded sheet thicknesses. The micro-CT analysis discovered that the ratios of defect volume to material volume remained low, and the manufacturing accuracy was high. Yang et al. [21] fabricated gradient G structures with different orientations using SLM to investigate the impact of gradient on fabrication fidelity. The results demonstrated that the fabrication

fidelity of SLM-built G structures depends on the inclination angle, relative density, and gradient direction. Wang et al. [22] prepared two sets of irregular porous scaffolds using SLM and showed that all internal and external struts were precisely fabricated. The porosity deviations between the models and the specimens were less than 4%, which satisfies the requirement of high-precision fabrication of porous materials. The abovementioned studies demonstrate that SLM can fabricate complex TPMS structures with sufficient precision.

Lattice structures are usually composed of struts or trusses, and such a structure has a common weakness [23]. Truss or strut structures cause stress concentrations and possible defects around the connections between truss elements, leading to the degradation of elastic and plastic properties [24] and causing the structure to collapse under lower applied loads [25, 26]. On the contrary, joints and nodes are absent in the TPMS structure. It was also found that the base material could greatly influence the deformation mode and mechanical properties of TPMS structures. For example, P, G, and N structures fabricated using Ti-6Al-4V as the base material underwent shear banding at large compressive strains and exhibited a stretching-dominated deformation mode [27]. In contrast, the structures using 316L steel as the base material exhibited a bending-dominated deformation mode [28]. More importantly, the topology of TPMS lattices could influence mechanical characteristics. In this regard, AlMahri et al. [29] compared five lattice structures (P, G, I-WP, D and F-K), and found that the D structure showed the highest plateau stress and the best energy absorption characteristics. Al-Ketan et al. [11] studied the P, G, D, and I-WP lattices and found that the D lattice exhibited the highest plateau stress. Yin et al. [30] studied the lattice structures of P, G, I-WP and F-RD and found that F-RD has the highest plateau stress and the best energy absorption. While the P, G, D, and I-WP structures have been extensively explored [31], limited studies have been conducted on the F-RD, F-K, N and I_2-Y^{**} structures. Since the fabrication processes, experimental setups, and mechanical characterization methods of the existing studies might not be completely consistent, the comparison results cannot be simply combined. To further explore the most efficient lattices, the mechanical properties of eight TPMS structures were comprehensively compared under the same conditions, aiming to complement the findings in existing studies.

The finite element (FE) method has commonly been utilized to numerically predict the mechanical properties such as compressive strength [32, 33], energy absorption [34], stress distribution [35] and anisotropy [36] of TPMS lattices, which can help to better understand the deformation behavior [37, 38] and mechanisms [39, 40]. Considering the simulation accuracy and computational efficiency, selecting a suitable element type is required. In this respect, Jia et al. [41] found that the multi-layer models meshed with the shell elements exhibited lower accuracy for simulating the compressive response of the P lattice structure with non-uniform shell thickness. Therefore, a solid element model is preferred for numerical simulation. Wang et al. [42] conducted a numerical investigation on G lattice cylindrical shell (LCS) specimens that were discretized using four-node quadrilateral shell elements with reduced integration (S4R). The results indicated that the calculated force-displacement curve exhibited an overall good consistency with the experimental results in all stages except the densification stage. Maskery et al. [43] utilized voxelized hexahedral elements for three TPMS structures and found that the established FE models cannot fully capture the deformation mechanisms in the experiment.

While element types could significantly impact the numerical result, there are limited studies on comparing different element types for the complex geometry of TPMS structures [44]. Further, to the authors' best knowledge, this has not been explored for the mechanical properties and energy absorption of TPMS structures under large deformation. Therefore, in this study, various meshing strategies and element types are compared and evaluated systematically for TPMS structures under large deformation.

The remainder of the paper is organized as follows. In Section 2, the design method of the TPMS lattice structure is introduced, and the quality of fabricated samples is evaluated. Section 3 investigates the mechanical properties of eight sheet-type TPMS lattice structures with different relative densities experimentally under quasi-static loading conditions. In Section 4, five meshing strategies are systematically investigated in terms of modeling ease, computational efficiency, data management, and simulation accuracy. The conclusions drawn from this study are given in Section 5.

2. Design of TPMS lattice structures and sample fabrication

In this Section, the design of eight TPMS lattices is given. Following that, the sample fabrication is presented, and the quality of fabricated samples is evaluated to ensure the reliability of the data.

2.1 Design of TPMS lattice structures

TPMS can be approximated with periodic surfaces expressed in simple trigonometric functions. The surfaces of eight TPMS lattice models studied herein are expressed using level-set formulas, as shown in Table 1 [45].

Table 1 Level-set formulas of eight TPMS sheet lattice models.

TPMS	Level-set formulas
P	$\emptyset_P(x,y,z) = cos(X) + cos(Y) + cos(Z) = c$
G	$\emptyset_G(x,y,z) = sin(X)\cdot cos(Y) + \sin(Z)\cdot cos(X) + \sin(Y)\cdot cos(Z) = c$
D	$\emptyset_D(x,y,z) = cos(X)\cdot cos(Y)\cdot cos(Z) - \sin(X)\cdot \sin(Y)\cdot \sin(Z) = c$
I-WP	$\emptyset_{I-WP}(x,y,z) = 2[cos(X)\cdot cos(Y) + cos(Y)\cdot cos(Z) + cos(Z)\cdot cos(X)] - [cos(2X) + cos(2Y) + cos(2Z)] = c$
F-K	$\emptyset_{F-K}(x,y,z) = cos(2X)\cdot sin(Y)\cdot \cos(Z) + \cos(X)\cdot \cos(2Y)\cdot \sin(Z) + \sin(X)\cdot \cos(Y)\cdot \cos(2Z) = c$
N	$\emptyset_N(x,y,z) = cos(X) + \cos(Y) + \cos(Z) + 3cos(X)\cdot cos(Y)\cdot cos(Z) = c$
I_2-Y**	$\emptyset_{I_2-Y^{**}}(x,y,z) = -2[\sin(2X)\cdot \cos(Y)\cdot \sin(Z) + \sin(X)\cdot \sin(2Y)\cdot \cos(Z) + \cos(X)\cdot \sin(Y)\cdot \sin(2Z)] + cos(2X)\cdot cos(2Y) + cos(2Y)\cdot cos(2Z) + cos(2Z)\cdot cos(2X) = c$
F-RD	$\emptyset_{F-RD}(x,y,z) = 4cos(X)\cdot cos(Y)\cdot cos(Z) - cos(2X)\cdot \cos(2Y) - cos(2X)\cdot cos(2Z) - cos(2Y)\cdot cos(2Z) = c$

Here, $X = \frac{k\cdot 2\pi}{l}\cdot x$, $Y = \frac{k\cdot 2\pi}{l}\cdot y$, $Z = \frac{k\cdot 2\pi}{l}\cdot z$. l represents the dimensions of the whole lattice structure, and k controls the number of unit cells in the x-, y-, and z-directions. The surface offset is determined by parameter c. The volume of the lattice structure is represented in Fig. 1(a) by the region produced by the two isosurfaces with positive and negative c. In this study, $l = 16$ and $k = 4$, which means that the designed samples have a dimension of 16mm × 16mm × 16mm with 4 × 4 × 4 unit cells. The 4 × 4 × 4 cell arrangement was considered sufficient to study the mechanical properties of the periodic TPMS structures [30].

Three relative densities (20%, 30%, and 40%) were designed for the eight TPMS lattice structures, and the designed relative densities (ρ) are given by:

$$\rho = \frac{V_{lattice}}{V_{solid}}, \tag{1}$$

where $V_{lattice}$ is the volume of the space formed by the offset of the isosurface and V_{solid} is the volume of the whole cube [29] (see Fig. 1(b)). It is observed that the relative density can be controlled by changing the *c* value. The *c* values used for the eight TPMS lattice structures with three different relative densities are listed in Table 2. Based on the calculated *c* value, the STL files for different TPMS structures were generated by MATLAB code, and then the CAD models were generated, as shown in Fig. 1(f).

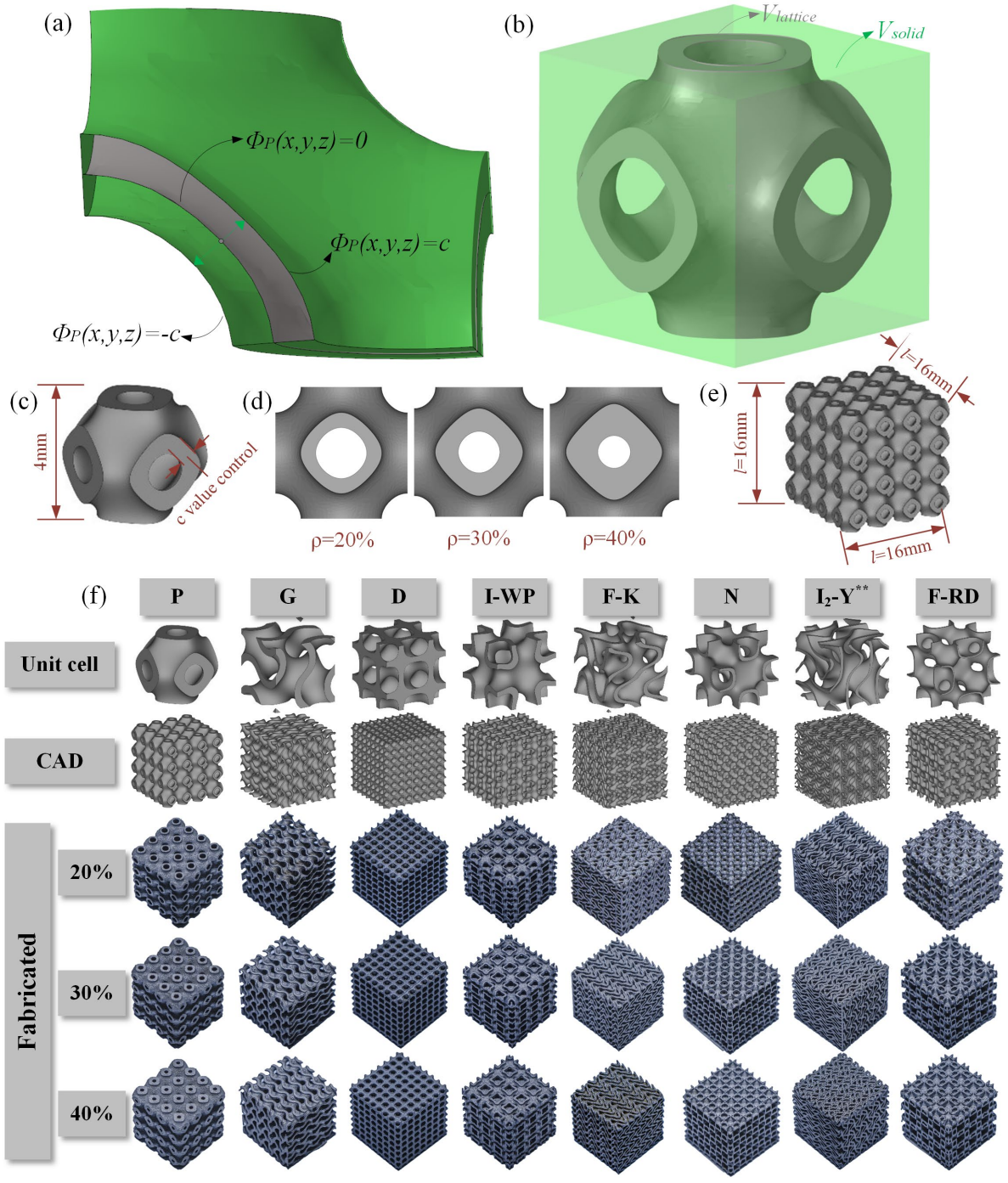

Fig. 1. The design of TPMS lattice structures. (a) The P lattice structure generated by the isosurfaces $\emptyset_P(x,y,z) = \pm c$. (b) Calculation of relative density of P lattice structure. The ratio of the volume of the lattice structure to the volume of the cube was defined as the relative density of the lattice structure. (c) The design dimension of the side length of the P unit cell, i.e., 4mm. (d) P unit cells of three relative densities, i.e., 20%, 30% and 40%, respectively. (e) Four unit cells were arranged in each direction, leading the overall dimension of the P lattice structure to 16mm × 16mm × 16mm. (f) CAD models of eight TPMS structures and

fabricated samples of three relative densities.

Table 2 *c* values used for eight TPMS lattice structures at three relative densities.

Relative density (%)	P	G	D	I-WP	F-K	N	I_2-Y**	F-RD
20	0.350	0.309	0.172	0.754	0.202	0.294	0.547	0.464
30	0.525	0.461	0.257	1.129	0.303	0.441	0.797	0.693
40	0.699	0.614	0.328	1.503	0.403	0.588	1.016	0.922

2.2 Sample fabrication

Due to the excellent ductility of 316L steel, it was selected for fabricating TMPS lattices in this study. The chemical composition of the 316L steel powder is shown in Table 3. The powder particle sizes were narrowly distributed between 20 μm (D10) and 55 μm (D90). The powder's scanning electron microscopy (SEM) image was acquired, as shown in Fig. 2(a). The results indicated that the powder has good sphericality and uniform particle size distribution.

Table 3 Chemical composition of 316L stainless steel powder.

Element	Fe	Cr	Ni	Mo	Mn	Si	C	P	S	O
wt. %	/	16-18	10-14	2-3	0-2	0-1	0-0.3	0-0.045	0-0.03	0-0.1

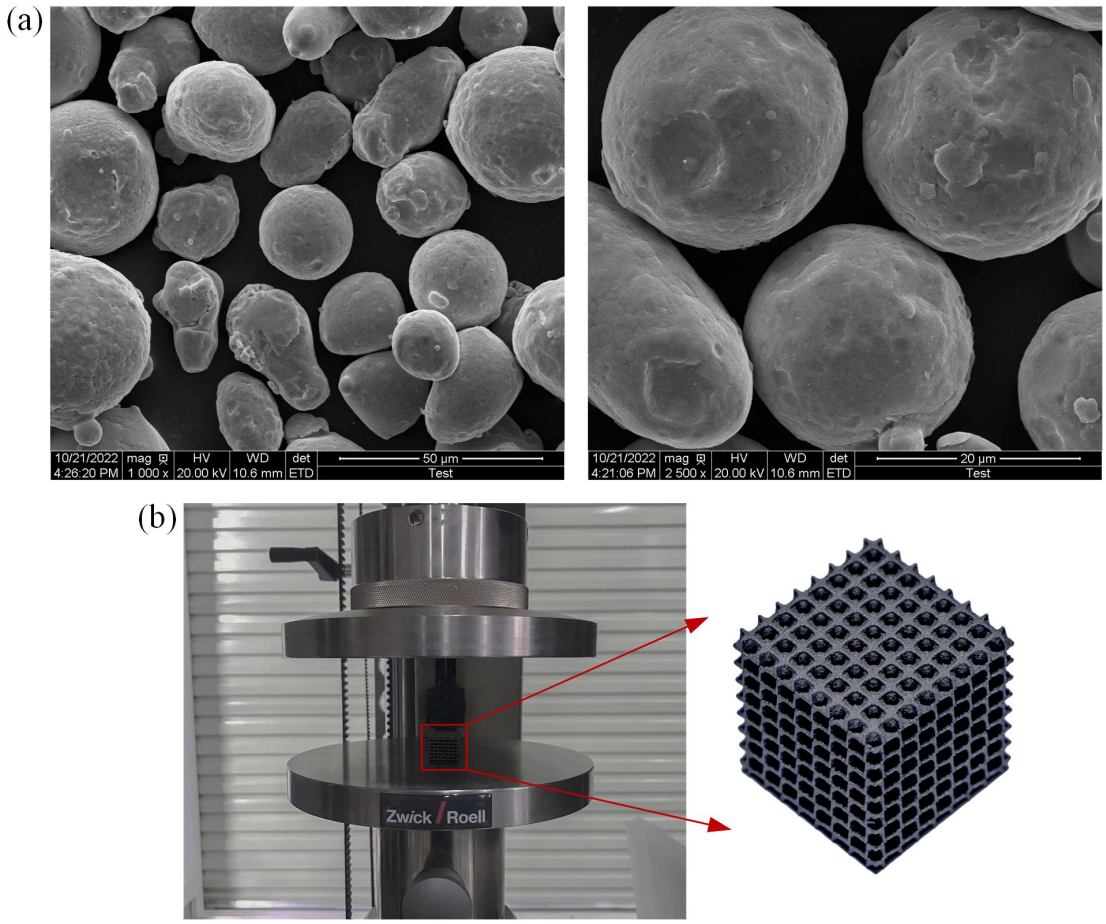

Fig. 2. SEM image of 316L stainless steel powder and photo of the testing facility. (a) 316L stainless steel powder in the particle size distribution at 20µm and 50µm scale, respectively. The powder had good sphericity and uniform particle size distribution. (b) Zwick AllroundLine Z250 universal material testing machine. All quasi-static compression was done on the testing machine and force-displacement data was recorded.

The SLM technique was used to fabricate the TPMS lattice structures using the printer EOS M290 (EOS GmbH, Krailing, Germany). The argon atmosphere used for the SLM process had less than 0.1% oxygen concentration. The process parameters were as follows: a scanning speed of 1200 mm/s, laser power of 280 W, scanning pitch of 0.14 mm, and a layer thickness of 30 µm. The fabricated lattice structures were removed from the base plate by wire electrical discharge processing and finally subjected to a 2-hour heat treatment at 800°C, followed by chamber cooling. The fabricated samples are shown in Fig. 1(f).

2.3 Assessment of sample fabrication

The samples were labeled with "structural abbreviation + relative density". For example, the P lattice structure with a designed relative density of 20% is described as P20, and I2-Y** lattice structure with a designed relative density of 40% is expressed as I2Y40. The actual relative densities ρ^* of the fabricated samples were greater than the designed relative densities, as shown in Fig. 3(a). The degree of deviation between the designed ρ and actual relative density ρ^* varied for different lattice structures. Specifically, the P lattice structure attained the smallest overall deviation, and the F-RD lattice structure had the largest overall deviation. Because different TPMS structures had different internal complexity, the residual particles attached to their surfaces were also different. For this purpose, SEM images of the samples were acquired. Fig. 4(a) shows the SEM images of D20, scanned from its top, bottom, and side surfaces. It can be found that the top and bottom surfaces of the sample were printed with higher quality and could reproduce the model features.

On the contrary, the side surfaces of the sample were of poor quality, with incomplete connections at some sites. Meanwhile, it was observed that a large amount of powder was attached to the side surfaces, resulting in its edges not being smooth, while a small amount of powder was also attached to the top and bottom surfaces. The same observation was also found in previous studies [11, 28, 29, 46-48]. Due to a large amount of heat released during the solidification of the printed layer, some adjacent powders melt and stick more easily to the side surfaces of the sample, forming a distinct rough morphology.

In addition, the particles adhering to the surface after the heat treatment process were more difficult to remove [49], which may be another important reason for making the actual relative density greater than the designed one [50]. Interestingly, the deviation was more pronounced for the samples with lower relative density or thinner walls due to the manufacturing error of the SLM process. Moreover, the relationship between the surface area of the samples and the relative density deviation was further explored, as shown in Fig. 3(b). The relative density deviation and the surface area generally showed a positive correlation, which implies that lattice structures with a smaller surface area have less powder attached to their surface. The P lattice structure was of the highest printing quality, followed by the G, I-WP, D, and N lattice structures. Notably, the F-RD and F-K lattice structures had a wide

deviation range, and the fabrication quality was very sensitive to the relative density. Strikingly, for the F-RD lattice structure with a large relative density, the pores of the fabricated sample were found much smaller than the pores of the design model, making it impossible to remove more powder from the internal structure, leading to higher deviation at a relative density of 40%, as shown in Fig. 4(b).

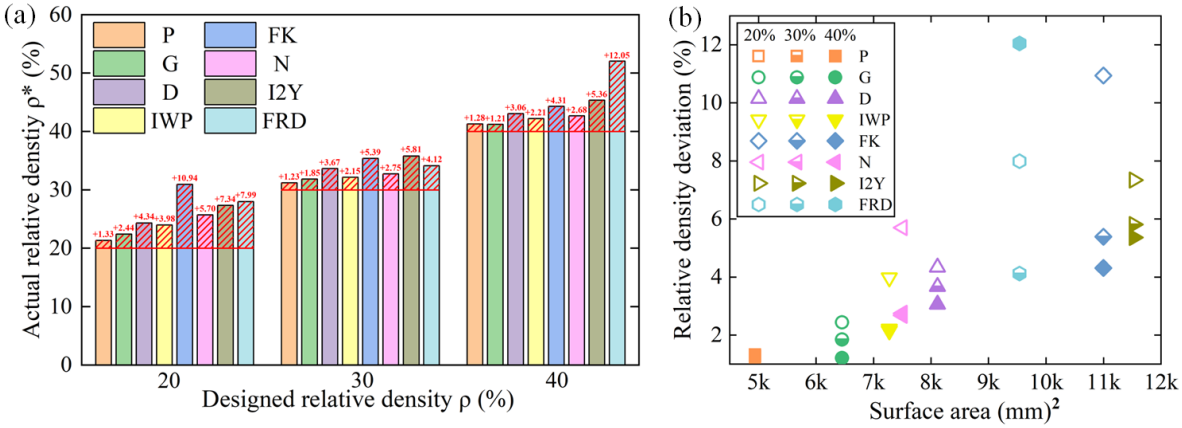

Fig. 3. (a) The deviation between the designed relative density ρ and the actual relative density ρ^* for different TPMS structures. $\rho^* > \rho$ due to the adherence of powder on the sample surface. The deviation was larger for F-K and F-RD structures. (b) Relationship between surface area and relative density deviation. The structure with a larger surface area tended to attach more powder, resulting in a larger relative density deviation.

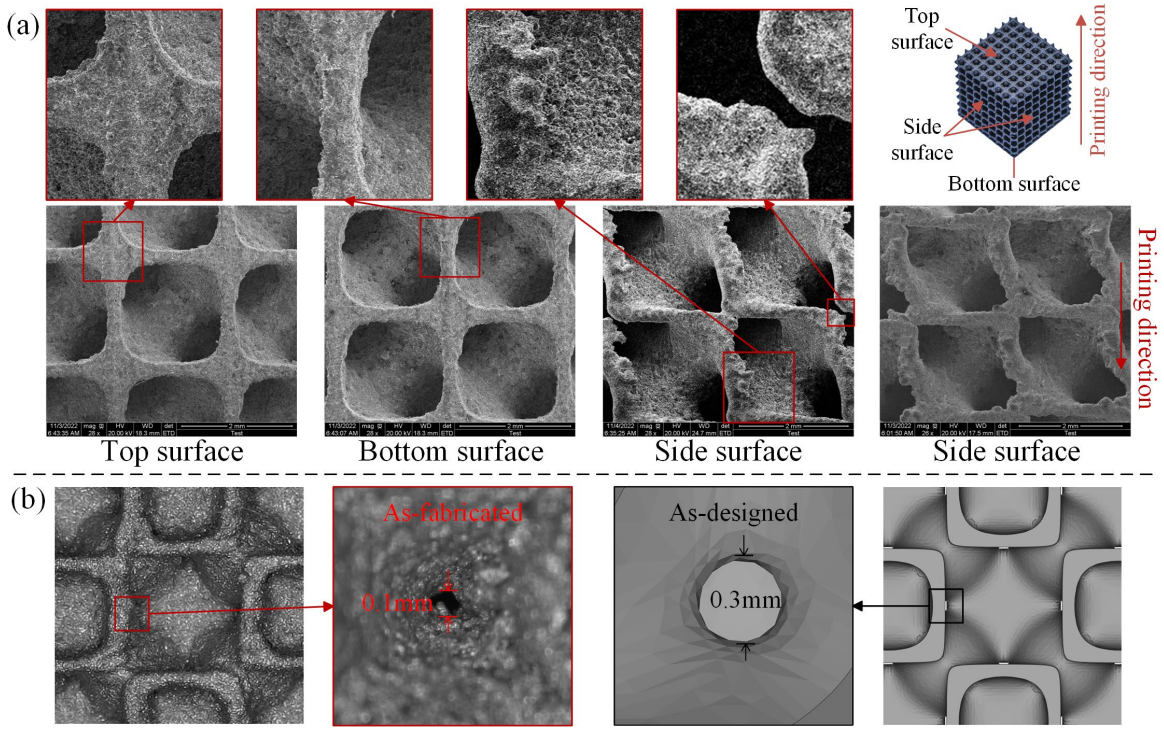

Fig. 4. (a) SEM images of the top, bottom, and side surfaces of D20. A large amount of powder was attached to the surface of the fabricated sample, and the powder attachment to the side surface was more pronounced. The surface morphology of the top and bottom surfaces was better than that of the side surfaces. (b) SEM images of the fabricated sample and designed model of FRD40. The powder attached to the surface increased the thickness of the fabricated sample, resulting in the hole size of the fabricated sample being smaller than that of the designed model.

3. Experimental study

In this Section, the deformation behaviors and mechanical properties of the eight TPMS lattice structures are analyzed and discussed thoroughly.

3.1 Experimental condition

To characterize the quasi-static mechanical response of the fabricated samples, quasi-static compression was performed using a Zwick AllroundLine Z250 materials testing machine with a constant loading rate of 1.2 mm/min, as shown in Fig. 2(b). The compression direction was parallel to the build direction. The deformation process of the samples during quasi-static compression was recorded with a camera.

3.2 Stress-strain curve

Three tests were repeated for P and G lattice structures in this study. Figs. 5(a) and 5(b) showed the nominal stress-strain curves for the repeating samples of the two lattice structures at different relative densities. Here, the nominal stress was obtained by dividing the force by the nominal cross-sectional area of the sample, and the nominal strain was calculated by dividing the displacement by the initial height of the sample [51]. A high degree of consistency was observed for the repeating experiments, making us confident that the fabricated samples could obtain highly reproducible testing results.

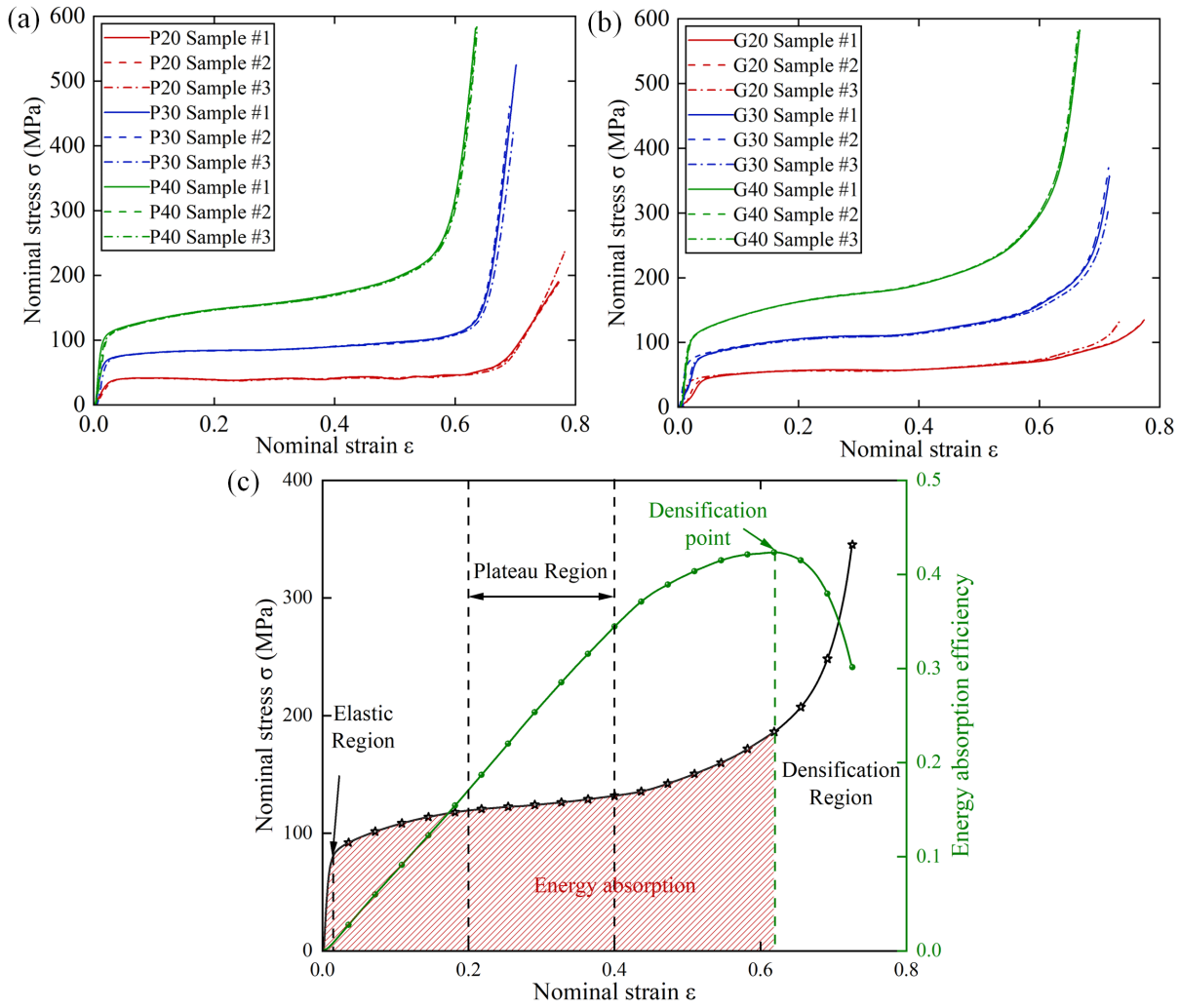

Fig. 5. Nominal stress-strain curves obtained from three repeat tests for (a) P and (b) G lattice structures at three relative densities. The stress-strain curves were highly overlapping, indicating the consistency of the obtained experimental data. (c) Nominal stress-strain curve of D30 under quasi-static compression, showing the typical response for all the lattices, with a smooth transition from the initial elastic phase to the plastic phase, followed by a plateau region with a slight increase in normal stress, and finally a densification region with a significant increase.

Fig. 5(c) shows the mechanical response of D30 under quasi-static compression. This typical mechanical response occurred for all the lattice structures with three relative densities, with a smooth transition from the initial elastic phase to the plastic phase, followed by a plateau region with a slight increase in normal stress, and finally a densification region with a significant increase in the curve.

The same lattice structure with different relative densities exhibited similar mechanical responses, as shown in Fig. 6. It was observed that the stress was stable, and its fluctuations were negligible due to the excellent ductility of 316L stainless steel, agreeing with the phenomenon that no cracks were observed in the samples during the quasi-static compression process.

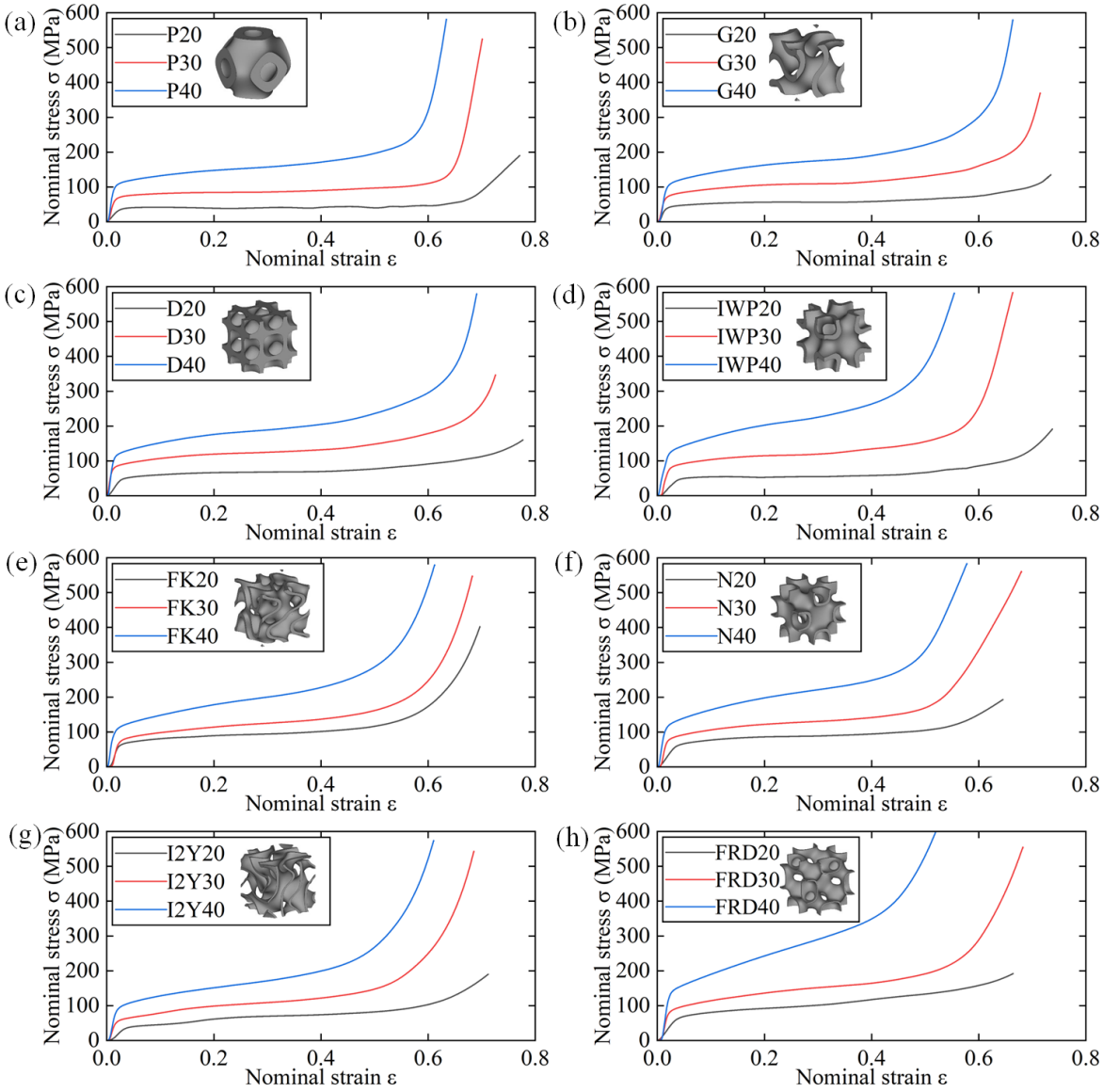

Fig. 6. Nominal stress-strain curves under quasi-static compression with designed relative densities of 20%, 30%, and 40% for (a) P, (b) G, (c) D, (d) I-WP, (e) F-K, (f) N, (g) I_2-Y^{**} and (h) F-RD lattice structures. Due to the excellent ductility of 316L stainless steel, the stress was stable and its fluctuations were negligible.

3.3 Deformation behavior

All quasi-static compression processes were recorded, as shown in Fig. 7. It was observed that the deformation behavior was mainly affected by the structural topology. In general, most of the TPMS structures collapsed in a homogenous deformation mode, which means each layer of unit cells was deformed simultaneously in the same manner. Interestingly, initial “X”-shaped double shear bands appeared in P20, and the unit cells on the diagonal experienced more severe deformation than the others (see Fig 7(a)). Initial single shear bands appeared in D20, and the unit cells on the diagonal were crushed locally (see Fig. 7(c)). For IWP20, at the beginning of compression, the middle layers collapsed while the other layers remained undeformed (see Fig. 7(d)). However, the excellent ductility of the 316L steel prevented the further development of the shear bands and local collapse, leading to the subsequent homogenous deformation mode. Furthermore, the shear banding and local collapse became less noticeable when the relative density increased to 30% and 40%. One possible reason for this is that the low relative density lattices were more sensitive to fabrication defects, more likely leading to local deformation. At larger relative densities, the mechanical performance might be less affected by fabrication defects and thus the lattices tended to take more advantage of the toughness of 316L.

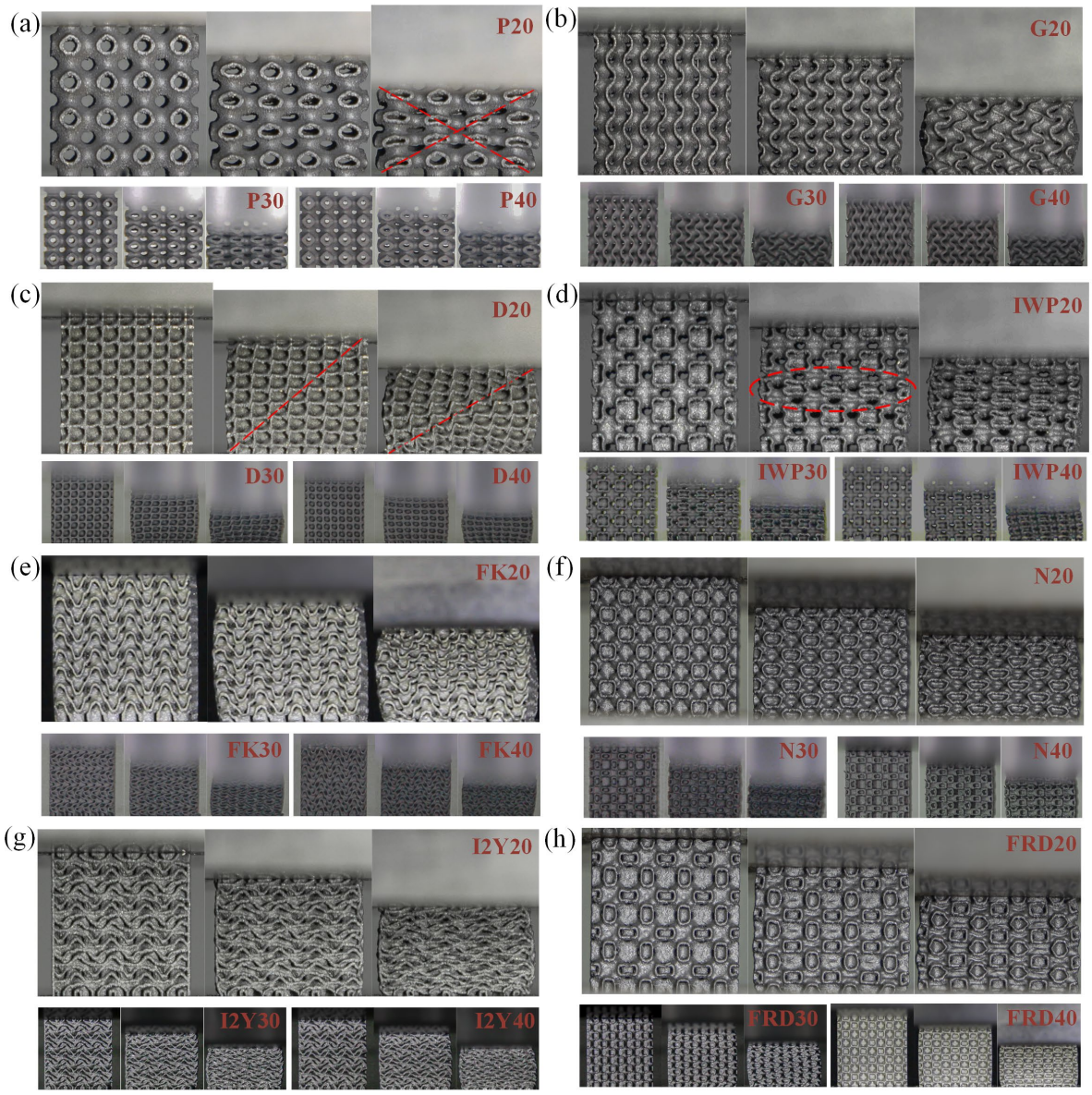

Fig. 7. Deformation of (a) P, (b) G, (c) D, (d) I-WP, (e) F-K, (f) N, (g) I_2-Y^{**}, and (h) F-RD structures at different strains. P20, D20 and IWP20 exhibited initial local "X"-shaped shear bands, initial single shear bands and local collapse, respectively. The excellent ductility of 316L steel prevented further development of shear bands and local collapse, leading to the subsequent homogenous deformation mode. Furthermore, the shear banding and local collapse became less noticeable when the relative density increased to 30% and 40%.

3.4 Energy absorption

Several important parameter indicators can be obtained from the stress-strain curve [52, 53]. The plateau stress (σ_{pl}) is determined by the average of nominal stress corresponding to the nominal strains of 0.2-0.4 [52] (see Fig. 5(c)). From the nominal stress-strain curve,

energy absorption and energy absorption efficiency can be calculated, and the onset of the densification region can be determined. As shown in Fig. 5(c), the energy absorption is expressed as the area under the nominal stress-strain curve and can be determined with integrals:

$$W_v = \int_0^{\varepsilon} \sigma(\varepsilon) d\varepsilon, \tag{2}$$

where W_v is the energy absorption and $\sigma(\varepsilon)$ is the stress related to strain ε. The energy absorption efficiency $\eta(\varepsilon)$ shown in Fig .5(c) can be determined by the following formula:

$$\eta(\varepsilon) = W_v/\sigma(\varepsilon). \tag{3}$$

The onset of the densification region can be determined when the energy absorption efficiency reaches the maximum as follows:

$$d\eta(\varepsilon)/d\varepsilon|_{\varepsilon=\varepsilon_D} = 0, \tag{4}$$

where ε_D is the strain of densification.

Excessive initial maximum force could be extremely harmful and should be considered seriously for practical applications [54]. Since all the lattice structures in this study did not show initial peak stresses, the plateau stresses were used to evaluate the mechanical strength. A combination of a high plateau stress and a large densification strain is always preferable for improving energy absorption. It should be noted that energy absorption before the strain of densification was calculated, i.e., $W = W_v|_{\varepsilon=\varepsilon_D}$ [55]. The relationship between mechanical properties and relative density is described by the Gibson-Ashby model [56], linking relative density to the mechanical properties of lattice structures [57]. The plateau stress σ_{pl} and the energy absorbed per unit volume W of the cellular structure can be characterized as a function of relative density using power laws according to the classical theory of cellular solids [11]:

$$\sigma_{pl}/\sigma_y = C_1 \rho^{*n_1}, \tag{6}$$

$$W/\sigma_y = C_2 \rho^{*n_2}, \tag{7}$$

where σ_y is the yield strength of the base material, C_i and n_i $(i = 1,2)$ were the geometric coefficients and exponents fitted to the specific structures, ρ^* is the actual relative density. The fitted curves were plotted in Figs. 8(a) and 8(c) and the fitting equations were given. All R^2 values of the fitting curves were greater than 0.99.

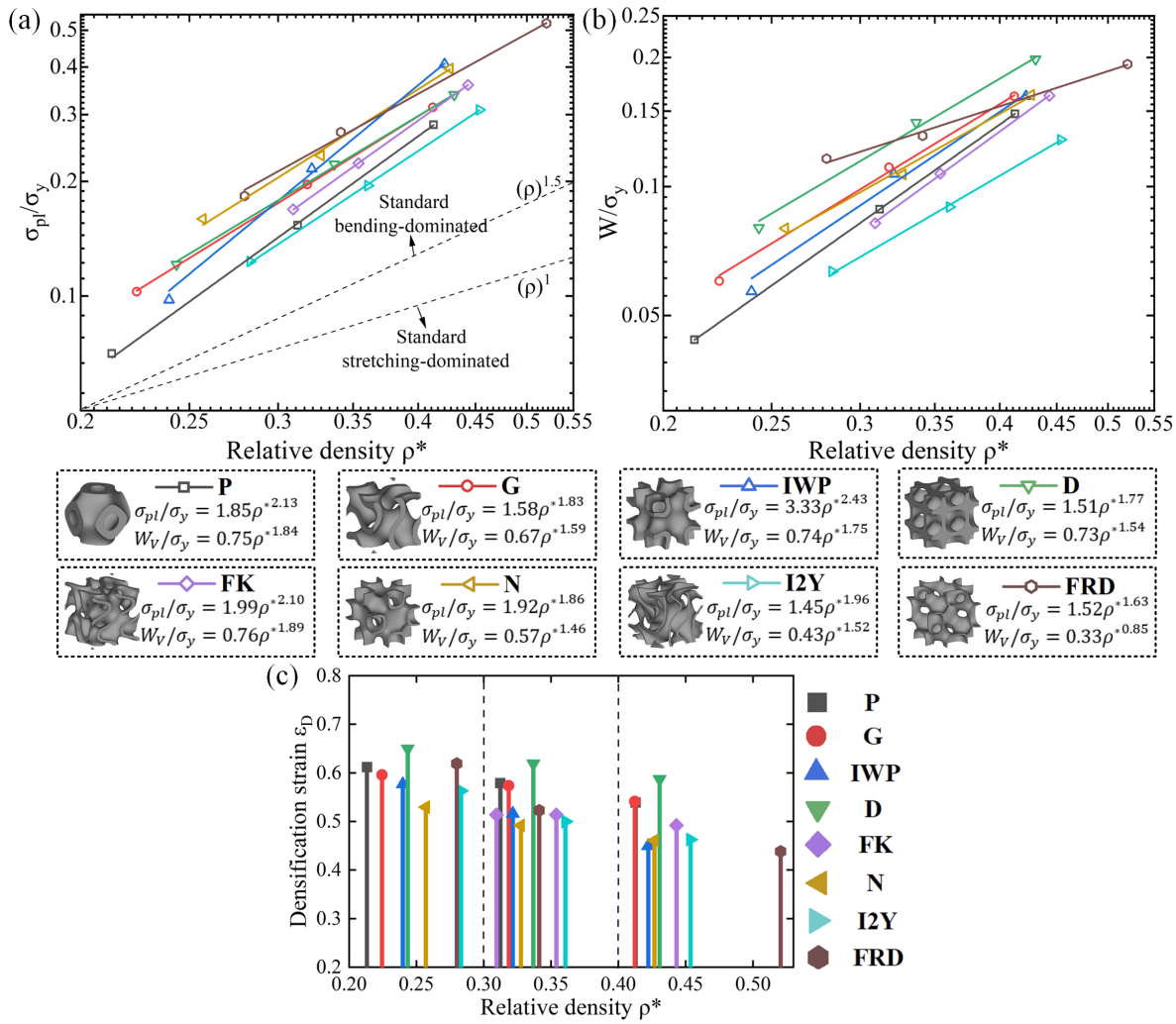

Fig. 8. Normalized mechanical properties with respect to the actual relative density: (a) plateau stress, with a fitting exponent greater than 1.5 for all structures, showing a bending-dominated deformation mode. (b) Energy absorption, with D and F-RD lattice structures showing the best energy absorption properties at relative densities greater and less than 30%, respectively. Among them, only the F-RD lattice structure had a fitting exponent of less than 1, indicating a significant advantage in lightweighting. (c) Densification strains. A larger relative density led to a smaller densification strain for all the lattice structures and the D structure had the largest densification strain.

When the fitting exponent n_1 is 1, the lattice exhibits a standard stretching-dominated mode, and when n_1 is 1.5, it exhibits a standard bending-dominated deformation mode [27]. From Fig. 8(a), the n_1 values of the eight lattice structures were in the range of 1.63-2.43, all greater than 1.5, showing a bending-dominated deformation mode. It is worth pointing out that the bending-dominated deformation mode is helpful for energy absorption [58]. The F-

RD lattice structure showed the highest plateau stress, and the fitting exponent n_1 was 1.63, which indicates that the F-RD lattice structure can show relatively high plateau stress under different relative densities. At the same time, due to its smallest fitting exponent, it could perform even better at low relative densities. It is worth noting that the I-WP lattice structure with the largest fitting exponent of 2.43 performed worse at lower relative densities and better at higher relative densities. The N lattice structure exhibited the second-highest plateau stresses, followed by the G and D lattice structures with nearly the same plateau stresses. The P and I_2-Y^{**} lattice structures obtained the lowest plateau stresses.

Fig. 8(b) compares the energy absorption for the eight lattice structures. The F-RD lattice structure showed the best energy absorption at low relative densities but lost its advantage at high relative densities because it was the only structure with a fitting exponent of less than 1. The other seven lattice structures' n_2 values were in the range of 1.63-2.43, showing a similar energy absorption trend. Interestingly, the D lattice structure possessed a high energy absorption at all the relative densities and exhibited a clear advantage at high relative densities.

Fig. 8(c) depicts the densification strains for all the samples with different relative densities. Generally speaking, the increase in the relative density of the sample implies an increase in thickness, inevitably leading to early contact between the walls during the quasi-static compression process. This explains the negative correlation between the relative density and the densification strain for all the structures. Moreover, the D structure showed the largest densification strain in the studied relative density range, followed by the P and G lattice structures. For the F-RD lattice structure, the densification strain was large when the relative density was less than 30% and significantly decreased as it increased, indicating that its densification strain is strongly influenced by the relative density. In contrast, the N and I_2-Y^{**} structures showed the lowest densification strain for all the relative densities.

According to the above analysis, the D lattice structure is advantageous in energy absorption at relative densities greater than 30% due to its large densification strain. On the other hand, the F-RD lattice structure shows better energy absorption at relative densities of less than 30% due to its large plateau stress. Therefore, the F-RD lattice structure has great potential in the application of lightweight energy-absorbing materials. The relationship

between mechanical properties and plateau stress was also described using the Gibson-Ashby model by Al-Ketan et al. [11]. In their study, D had the smallest fitting exponent of 1.53 among P, G, I-WP and D. and D exhibited the highest plateau stress in the relative density range of 16.5% to 24.5%. In another study by Yin et al. [30], the F-RD lattice provided a specific energy absorption of 32.47 kJ/kg, much higher than the P, G and I-WP structures. The present study generally agrees with these previous studies and provides insightful information by exploring various TPMS structures more comprehensively.

4. Numerical study

Five meshing strategies were used to model three TPMS structures in this study, including P, G, and F-K. The P lattice structure was selected because it is widely studied, and its unit cells have a high degree of spatial symmetry and are the easiest to model among the eight TPMS structures. The G and F-K lattice structures were selected because they are less symmetrical and their larger surface areas can lead to a thinner wall under the same relative density. The symmetry and wall thickness of the model affects the meshing strategies; therefore, different meshing strategies and element types may be required for different TPMS structures.

The shell, solid, and voxel models were studied. The two shell models were meshed with triangular and quadrilateral elements, respectively. Similarly, the two solid models were meshed with tetrahedral and hexahedral elements, respectively. As for the voxel model, only hexahedral elements were studied. These five meshing strategies were compared to identify the best finite element type for TPMS lattice structures in terms of modeling ease, computational efficiency, data management, and simulation accuracy.

4.1 Finite element modeling

This Section introduces the finite element modeling of TMPS lattices, including boundary conditions and material parameters. Moreover, five modeling strategies are presented.

4.1.1 Boundary conditions and material parameters

Finite element analysis was performed using ABAQUS/Explicit solver. The same boundary conditions were utilized for all the models (see Fig. 9(a)). The TPMS lattices were placed on a lower fixed, rigid plate and compressed by a rigid upper plate. The upper plate moved downward 12.8 mm at a constant velocity of 0.5 mm/s, corresponding to 80% of the samples' height. Mass scaling was not used, and automatic time incrementation was set during the calculation. In addition, the general contact algorithm and element-based surface were automatically defined by ABAQUS/Explicit, which included all entities in the model. Single-sided surfaces were defined for the two rigid plates, and double-sided surfaces were defined for the TPMS lattices. Furthermore, the rigid plates and the TPMS lattices were designated as master and slave surfaces, respectively, and a pure master-slave approach was applied to resist only penetrations of slave nodes into master facets.

In order to obtain accurate material parameters, three tensile samples were made using the same 316L stainless steel powder and tested under quasi-static tensile conditions. The elastic-plastic parameters were obtained using digital image correlation (DIC) [59], where Young's modulus is 145,000 MPa and Poisson's ratio is 0.3. The material model was defined as nonlinear isotropic hardening in the plastic region, and the stress-strain curves are shown in Fig. 9(b). It was observed that the three curves agreed well with each other, indicating that the material properties have good repeatability. To accurately simulate fracture behavior, damage modeling involves stress state-dependent ductile fracture [13], which is a challenging task in computational mechanics. Besides, ductile fracture may only occur when the plastic deformation of 316L stainless steel exceeds a certain threshold. It was observed that the excellent ductility of 316L stainless steel resulted in very minor damage. In previous studies (e.g., Zhang et al. [28] and Yin et al. [30]), numerical models could provide sufficiently accurate predictions of TPMS structures without considering material fracture or failure. Therefore, fracture modeling was not taken into account in this study.

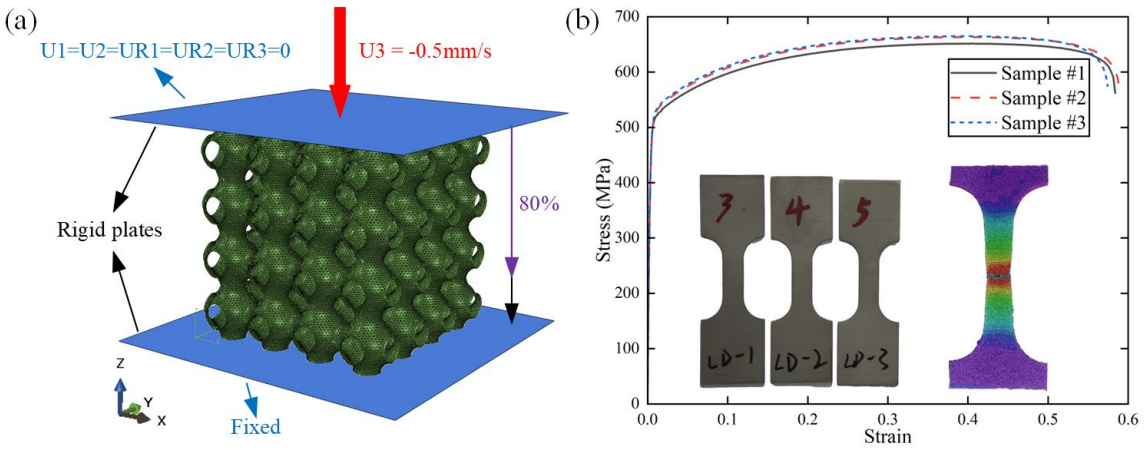

Fig. 9. (a) Boundary conditions used in the numerical study. The lower rigid plate was fully fixed in all degrees of freedom, while the upper rigid plate was loaded in the z-direction and fixed in the other five degrees of freedom. A constant velocity of 0.5mm/s was applied to the upper rigid plate to compress the fabricated samples up to 80% of their height. (b) Stress-strain curves of uniaxial tensile specimens made of 316L stainless steel. The strain field was calculated using the DIC technique to obtain more accurate material parameters. The three curves showed a high degree of agreement.

4.1.2 Five meshing strategies

The process of creating three finite element models is depicted in Fig. 10. For shell and solid models, STL files were generated by executing the related MATLAB codes. Then, the meshing operation was performed using commercial finite element pre-processor HyperMesh. For the voxel model, the solver input (INP) file was generated directly by executing the related MATLAB code.

In this study, the shell models were discretized automatically with two types of elements separately: triangular elements and quadrilateral elements. The meshing was performed on a unit cell and then the elements were repeated in the x-, y-, and z-directions to improve the meshing efficiency and symmetry characteristics.

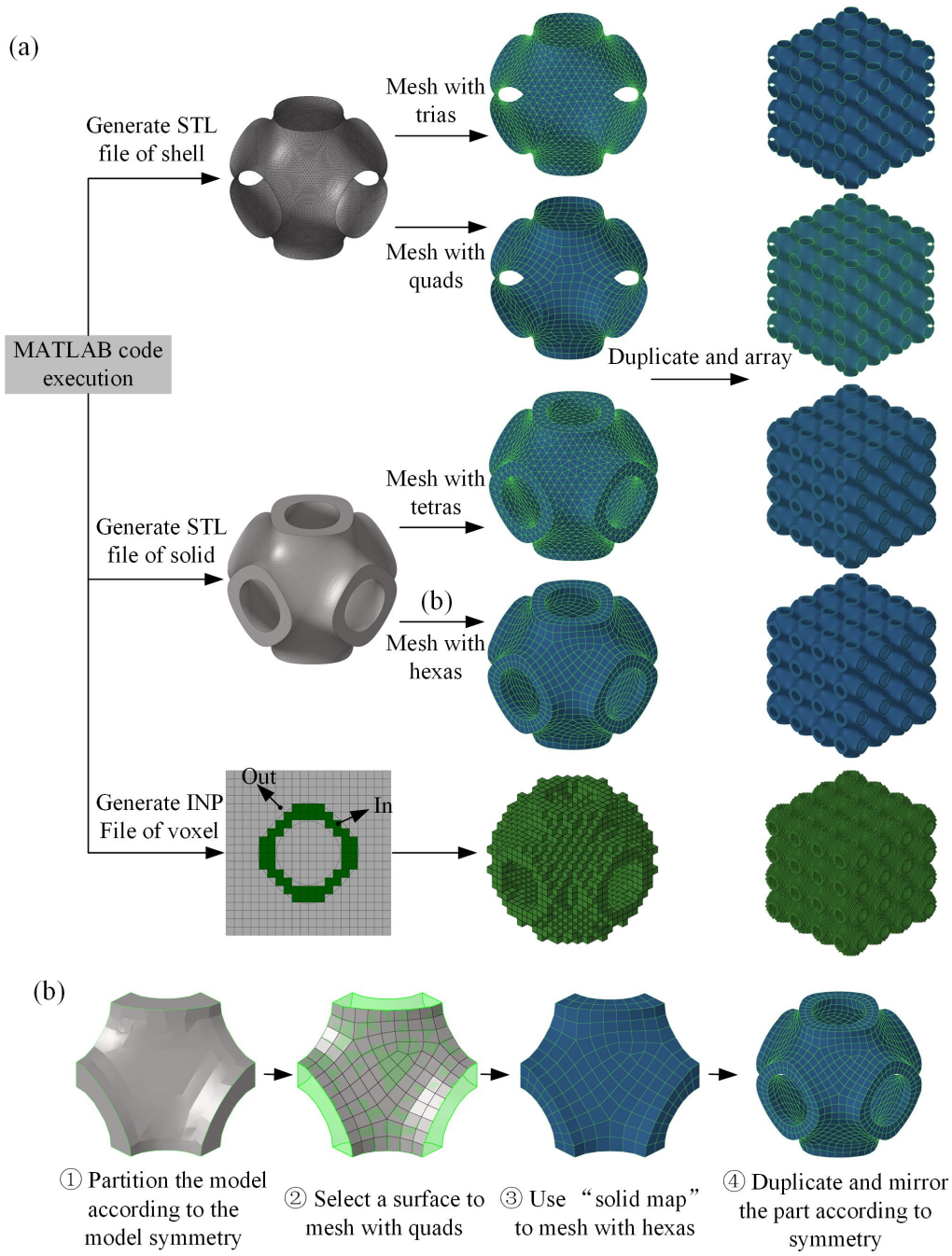

Fig. 10. (a) Shell, solid, and voxel modeling processes. The unit cells were generated by executing the MATLAB code, and the FE models were created by duplicating and arraying after the unit cell was meshed. (b) The detailed meshing process for the hexahedral element model of a P unit cell. The process included cutting the model according to symmetry, meshing a surface with the quadrilateral elements, mapping to mesh with hexahedral elements, and duplicating and mirroring to generate a unit cell model.

Similar to the shell models, two solid models were meshed with tetrahedral and hexahedral elements, respectively. For the tetrahedral elements, an automatic procedure

provided in Hypermesh was utilized. However, a lot of manual meshing operations were required for the hexahedral elements, which relies on expert experience. One example showing the detailed steps for meshing with high-quality hexahedral elements for a unit cell was illustrated in Fig. 10(b), including:

① Partition the unit cell into mappable solids according to the model symmetry.

② Select one of the two opposite surfaces to mesh with the quadrilateral elements.

③ Extrapolate the 3D solid map mesh with hexahedral elements from the existing quadrilateral elements.

④ Create the unit-cell model by duplicating and mirroring operations.

The modeling approach of the voxel model is shown in Fig. 10(a). During voxelization, the geometry of a surface was converted into a bit-by-bit 3D array, and the array could be mapped directly to a hexahedral mesh [44]. First, a 3D uniform mesh embedded in the solid model was defined. Along the three orthogonal directions, for each voxel, determine whether the voxel is inside or outside the solid model. Then, the elemental information of the voxel inside the solid model was written to the INP file by MATLAB code. Finally, information such as material properties, boundary conditions, and analysis steps was written into the INP file to generate the complete voxel model.

Table 4 summarizes the five meshing strategies. The model's mesh size is critical to balance computational accuracy and efficiency. Convergence studies were performed for all the FE models, as shown in Fig. 11. Generally, as the mesh size decreased, the stress level decreased until it stabilized when the mesh size could be judged to have converged. The converged mesh sizes were adopted in the FE models, as shown in Table 4.

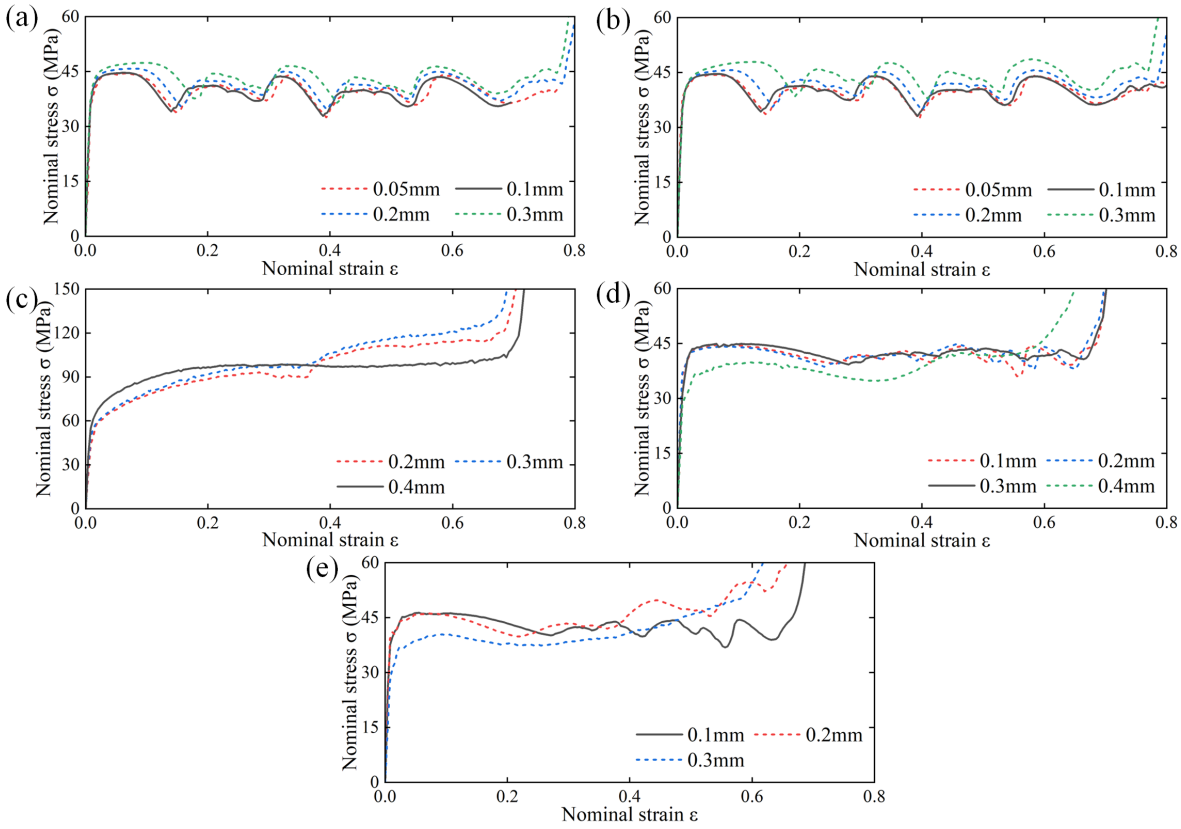

Fig. 11. The nominal stress-strain curves for convergence analysis of (a) S3, (b) S4, (c) C3D4 (solid), (d) C3D8 (solid) and (e) C3D8 (voxel). The mesh size of the triangular element, quadrilateral element, and voxel hexahedral element was considered converged at 0.1mm, and the mesh sizes of the tetrahedral element and hexahedral element in the solid model were 0.4mm and 0.3mm, respectively.

Table 4 Five meshing strategies used in ABAQUS/Explicit.

Model	Mesh type	Element type	Element size	Remark
Shell	Triangular	S3	0.1	3-node triangular general-purpose shell
	Quadrilateral	S4	0.1	4-node doubly curved general-purpose shell
Solid	Tetrahedral	C3D4	0.4	4-node linear tetrahedron
	Hexahedral	C3D8	0.3	8-node linear brick
Voxel	Hexahedral	C3D8	0.1	8-node linear brick

4.2 Comparison of different meshing strategies

In this Section, the above meshing strategies are compared in terms of modeling ease, computational efficiency, data management, and accuracy.

4.2.1 Modeling ease

The different meshing strategies were described in detail in Section 5.1. The voxel-based approach can generate a lattice model consisting of almost any cell type [60] and voxelization does not require much attention to mesh quality due to its mesh characteristics. Modeling is easiest since node and element numbers are directly generated by MATLAB code and written into INP files.

The shell models can be automatically meshed in HyperMesh. The P lattice structures with the smallest local curvature can be meshed directly and automatically. G and F-K have larger local curvatures, which need to be split into several parts manually and then meshed one by one automatically to ensure their mesh quality. Triangular elements have advantages over quadrilateral elements for fitting surfaces, and thus it is easier to generate higher-quality triangular elements.

The solid mesh model with tetrahedral elements was relatively easy to build because the tetrahedral element models can be meshed automatically in HyperMesh. However, there is no automatic function for hexahedral elements, and the creation of solid models with hexahedral elements requires many skills. Especially for models with large local curvature, much effort is needed to achieve high-quality meshes if not impossible. Another problem with solid models is that the node arrangement at the boundary of unit cells is more difficult than in other models. The node arrangement on opposite boundary faces needs to be identical for node connectivity at the boundary of unit cells in the tessellated mesh. Among the three TPMS lattice structures, only P20 was successfully modeled with hexahedral elements. As for FK, and G, their models do not have the same high degree of symmetry as the P structures and their unit cells have a large local curvature, leading to a huge difference between the opposite surfaces in terms of shape and area, especially for thick-walled (or high relative density) structures. This difference usually caused the failure of mapping from quadrilateral to hexahedral elements.

4.2.2 Computational efficiency and data management

Taking P20 as an example, the computational time and output file size (data management) of different meshing strategies were counted under the same field output, as shown in Table 5. All these models were executed on a computer with i5-CP11400F@2.60GHz CPU and 16GB RAM. It can be observed that computational efficiency is closely related to the number of degrees of freedom (DOF) and the number of elements. Considering the mesh convergence, the solid element contains the least number of elements and DOF, and, therefore, is the most computationally efficient and the smallest size of the output file. Next, S3 contains more elements and DOF than the solid model and S4, and has the lowest efficiency, while S4 is much more computationally efficient than S3. The voxel model contains the most elements and DOF, and its computational efficiency is higher than S3 but lower than S4. Obviously, data management is directly related to the number of elements. Using S3 and voxel elements needs more hard drive space for data storage, while S4 and solid elements are advantageous in data management.

Table 5 Computational time and data management of P20 with different approaches

Element type	Approach	Element number	DOF number	Computational time/h	Data management/GB
S3 (shell)	S3R	586,240	1,777,362	110.9	3.25
S4 (shell)	S4R	302,080	1,485,522	37.5	1.31
C3D8 (solid)	C3D8R	62,976	273,234	5.5	0.14
C3D4 (solid)	C3D4	145,536	201,522	3.5	0.32
C3D8 (voxel)	C3D8R	871,616	3,808,434	93.8	4.55

4.2.3 Simulation accuracy

To evaluate the simulation accuracy of the five meshing strategies, the simulated nominal stress-strain curves were compared, as shown in Fig. 15. It was observed that the simulation results of shell models (S3R and S4R) could reproduce the experimental response in the elastic-plastic and plateau regions for P20, G20, and FK20, but cannot capture the densification regions. In addition, neither the plateau nor the densification region could be predicted in the simulation of FK40. This is caused by the modeling error of shell elements,

which were set to have a constant thickness by matching the mass of the TPMS structure. However, the thickness of the actual model is not constant, which may have large deviations in the regions with large curvatures. The thickness was scaled down automatically due to contact algorithms in the simulation [61], so the instant of self-contact cannot be accurately predicted, especially in thick-walled structures. This was an important reason why the shell element could not predict the densification. Overall, the shell elements are considered accurate for low relative density or thin-walled lattice structures.

For the solid models, the tetrahedral (C3D4) element model showed large errors for all three TPMS lattice structures, as shown in Fig. 12. In contrast, the hexahedral elements (C3D8R) with reduced integration points could achieve good accuracy in both stress history and densification strain. However, meshing for hexahedral elements is very challenging and time-consuming. Thus, when hexahedral elements solid models cannot be created, one must resort to other meshing strategies.

For the voxel models, the simulation results of P20, G20, and FK40 showed high accuracy in both the plateau region and densification region, while the voxel model of FK20 exhibited a large error in the plateau region, as shown in Fig. 12(c). The thickness of FK20 at its thinnest area is only 0.1mm, resulting in weakly connected regions with only one or two voxel elements in the thickness direction, as shown in Fig. 13(a). In contrast, the thickness of FK40 at its thinnest area was 0.3mm, and there were enough voxel elements in its thickness direction. Therefore, the application of the voxel model in a thin-walled structure cannot capture the feature of the model, while the accuracy of the simulation by applying the voxel model in the thick-walled structure is satisfactory.

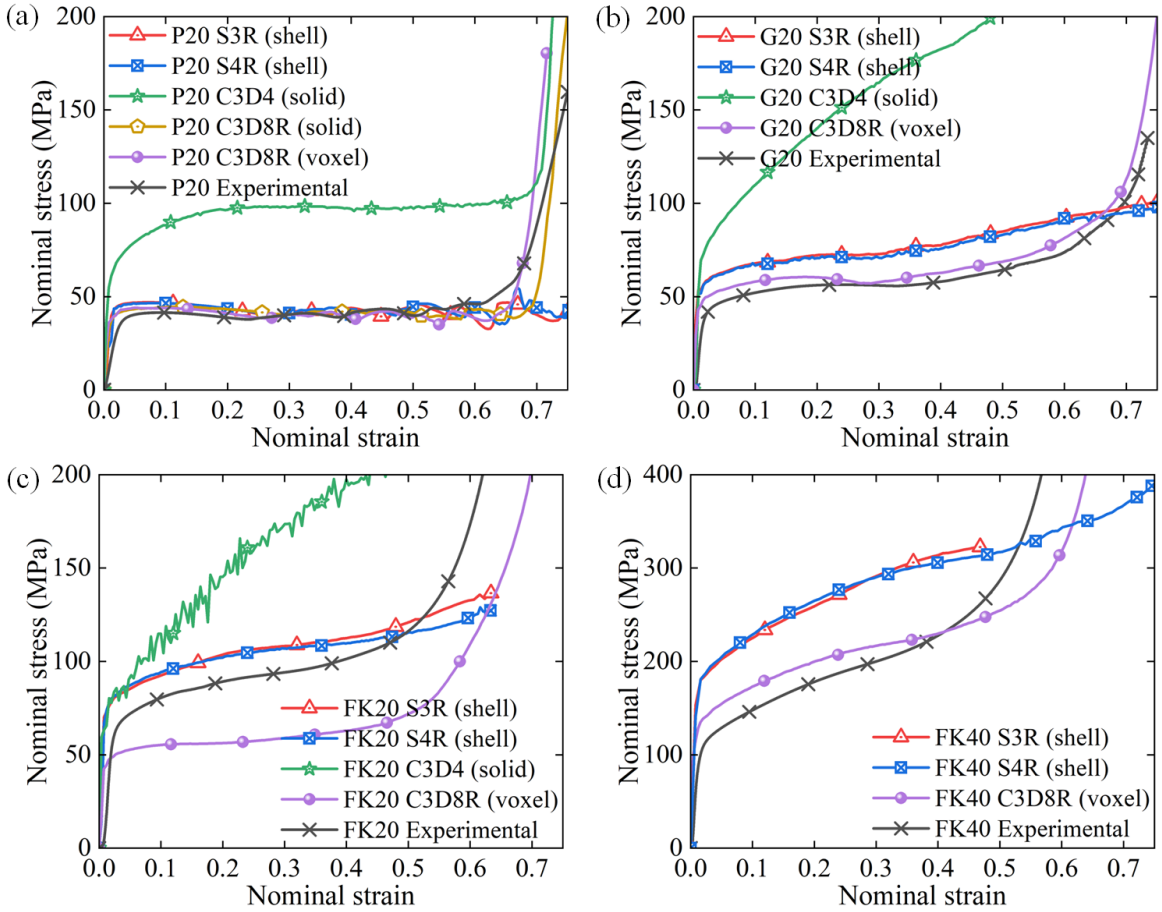

Fig. 12. The nominal stress-strain curves of (a) P20, (b) G20, (c) FK20, and (d) FK40. Shell elements could capture the stress level for the structures with small relative densities, but could not accurately predict the densification. Voxel models could accurately predict the mechanical behavior of large relative density structures at all the elastic-plastic, plateau, and densification regions.

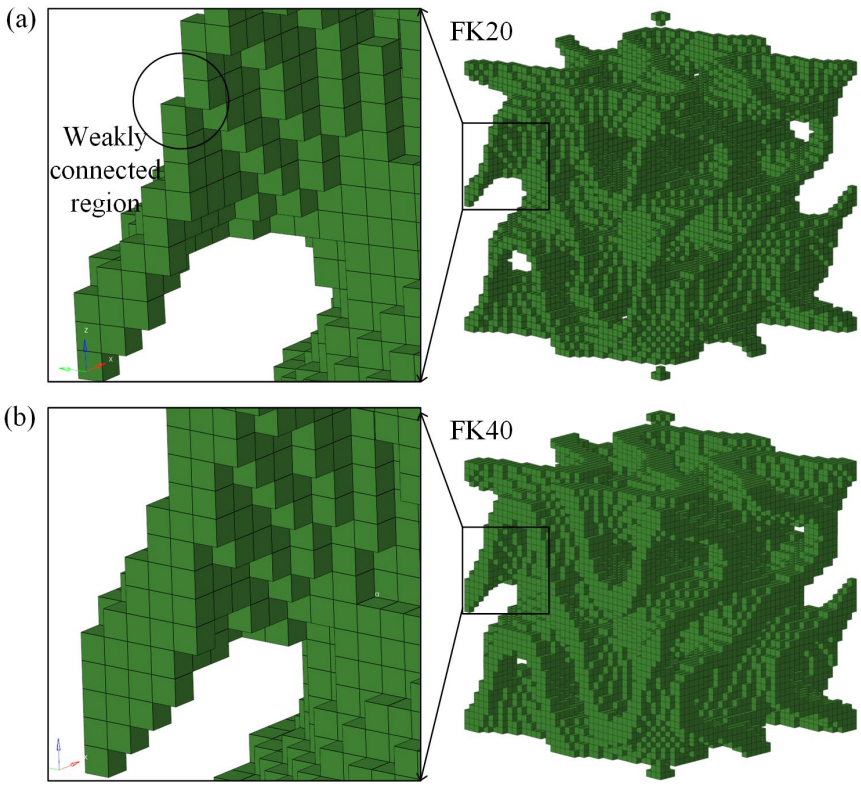

Fig. 13. Voxel model of unit cells of (a) FK20 and (b) FK40. FK20 had poor connectivity in some areas due to its thin wall, resulting in missing features due to mesh discretization. The connectivity became better as the thickness of the model increased.

To quantitatively compare the five meshing strategies, the plateau stresses of the nominal stress-strain curves in Fig. 12 were calculated, as shown in Fig. 14. The differences between the two shell models are insignificant, while C3D4 in the solid model shows a larger deviation and C3D8R shows the best accuracy for P20. Interestingly, the voxel C3D8R model exhibits different results for different lattice structures. Specifically, the voxel C3D8R model could yield acceptable results for P20, G20, and FK40, while there was a large error for FK20. In the simulation of FK20, the plateau stress of C3D8R in the voxel model was 61.92 MPa, much smaller than the experimental counterpart, 94.56 MPa. In contrast, in the simulation of FK40, the plateau stress of C3D8R in the voxel model was 216.21 MPa, consistent with the experimentally calculated value 201.00 MPa. This indicates the disadvantage of voxel models in lattice structures with low relative density or thin wall thickness.

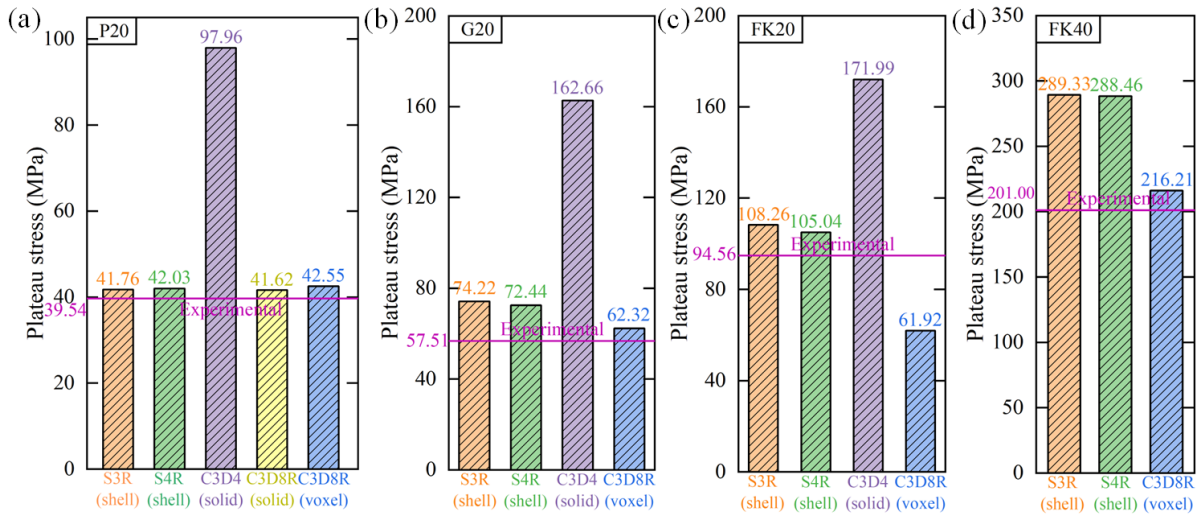

Fig. 14. Plateau stress for (a) P20, (b) G20, (c) FK20, and (d) FK40. The accuracy of C3D4 in solid models was unacceptable. Shell elements and voxel models were accurate at low and high relative densities, respectively.

In summary, for the solid models, the accuracy of C3D4 was not acceptable, and C3D8R showed the best accuracy in simulating the mechanical performance of P20. The shell models were preferred for low relative density or thin-walled structures and the voxel model was advantageous for high relative density or thick-walled structures.

4.2.4 Recommendations

The comparison between the five meshing strategies is represented by a radar chart in Fig. 15. The indicators are quantified on five scales, where "1" means the worst and "5" means the best. Overall, in solid models, C3D4 is not recommended due to poor accuracy and C3D8R is not recommended due to the difficulty of modeling. On the other hand, the voxel model and shell models have their advantages. Generally speaking, for relatively low-density or thin-walled structures, quadrilateral elements are recommended (see Fig. 15(a)) and for structures with high relative density, voxel elements are recommended (see Fig. 15(b)).

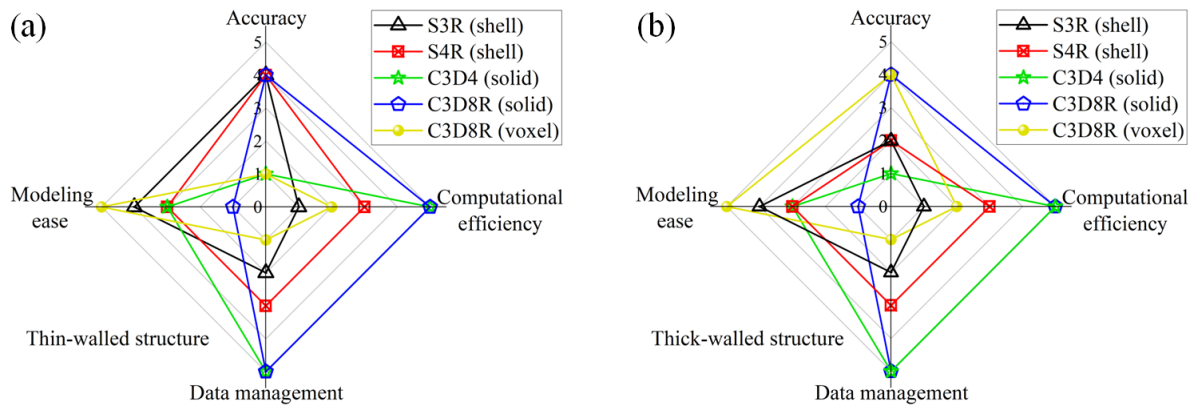

Fig. 15. Comparison between different meshing strategies for (a) thin and (b) thick-walled structures. Accuracy was considered the most important when comparing meshing strategies, followed by modeling ease. In thin-walled and thick-walled structures, S4R and voxel models showed the best overall performance, respectively.

4.3 Energy absorption mechanisms from numerical simulation

The energy absorption mechanisms of D and F-RD lattice structures were explored based on the simulations using the voxelization modeling method. To exclude the manufacturing error of adhesion powder, which cannot contribute to the mechanical property [50], the corresponding finite element models are built according to the designed relative density of the fabricated samples, as shown in Fig. 16(a).

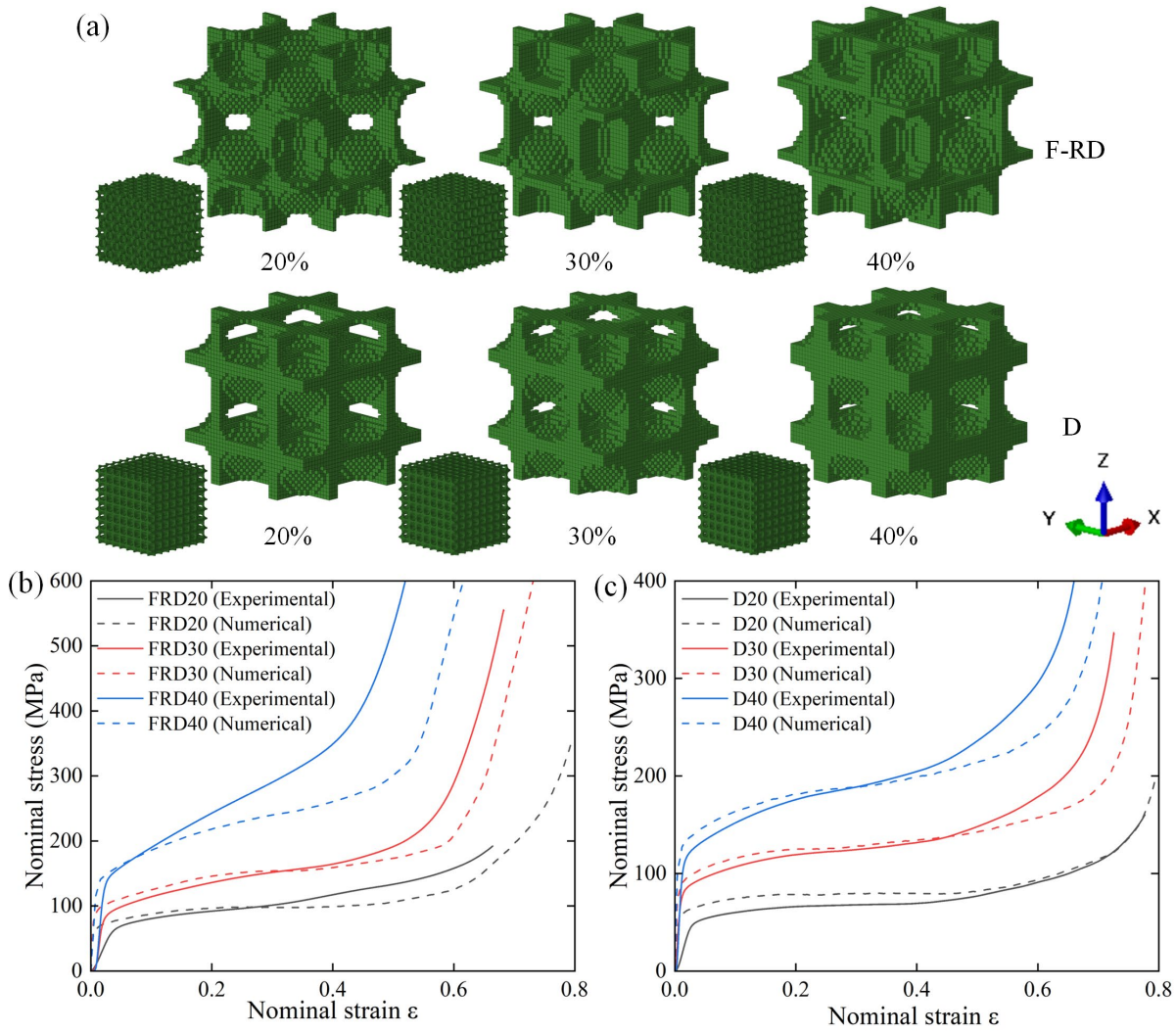

Fig. 16. Voxel models for (a) F-RD and D lattice structures with relative densities of 20%, 30%, and 40%, and experimental and numerical nominal stress-strain curves of (b) F-RD and (c) D lattice structures. The numerical and experimental results showed good consistency, and the stress of the F-RD structure was significantly higher than that of the D structure.

As shown in Figs. 16(b) and 16(c), the simulated nominal stress-strain curves for the F-RD and D lattice structures agreed well with the corresponding experimental results. Numerical simulations could reasonably capture the experimental response. However, the experimental results reached the densification stage earlier than the simulation curves in the densification region. This further confirms that the powder adhered to the experimental sample during manufacturing did not contribute to the mechanical properties, and the increased relative density led to earlier densification.

The von Mises stress distribution of the F-RD and D lattice structures was obtained by simulation, as shown in Fig. 17. Numerical simulations could predict the deformation behavior of the lattice structure. In agreement with the experiments, both lattice structures showed homogenous deformation behaviors.

At a relative density of less than 30%, the stress concentration in the D-lattice structure could be seen to occur mainly in the diagonal shear bands, and other regions of the lattice structure did not participate in carrying the external compressive load (see Fig. 17(b)). On the contrary, the F-RD lattice structure had a more uniform stress distribution, and more material of the lattice structure contributed to the load-carrying capacity, resulting in a higher level of plateau stresses (see Fig. 16(b)). Such a phenomenon resulted in the F-RD lattice structure absorbing more energy than the D lattice structure at relative densities of less than 30%.

At a relative density greater than 30%, the F-RD lattice structure prematurely underwent internal self-contact and entered the densification region early (see Fig. 17(a)). In contrast, the later internal self-contact of the D lattice structure allowed it to possess a greater densification strain than the F-RD lattice structure (see Fig. 17(b)). As a result, in the later stages of the compression process, the D lattice structure still could absorb energy, which is an important reason why the D lattice structure possessed a better energy absorption capacity than the F-RD lattice structure at relative densities of greater than 30%.

Overall, the F-RD lattice structure performed better due to more uniform stress distribution at a relative density of less than 30%, while the D lattice structure did due to a later internal self-contact at a relative density of greater than 30%. The simulation supplemented the experimental observation and further revealed the energy absorption mechanisms of TPMS lattice structures.

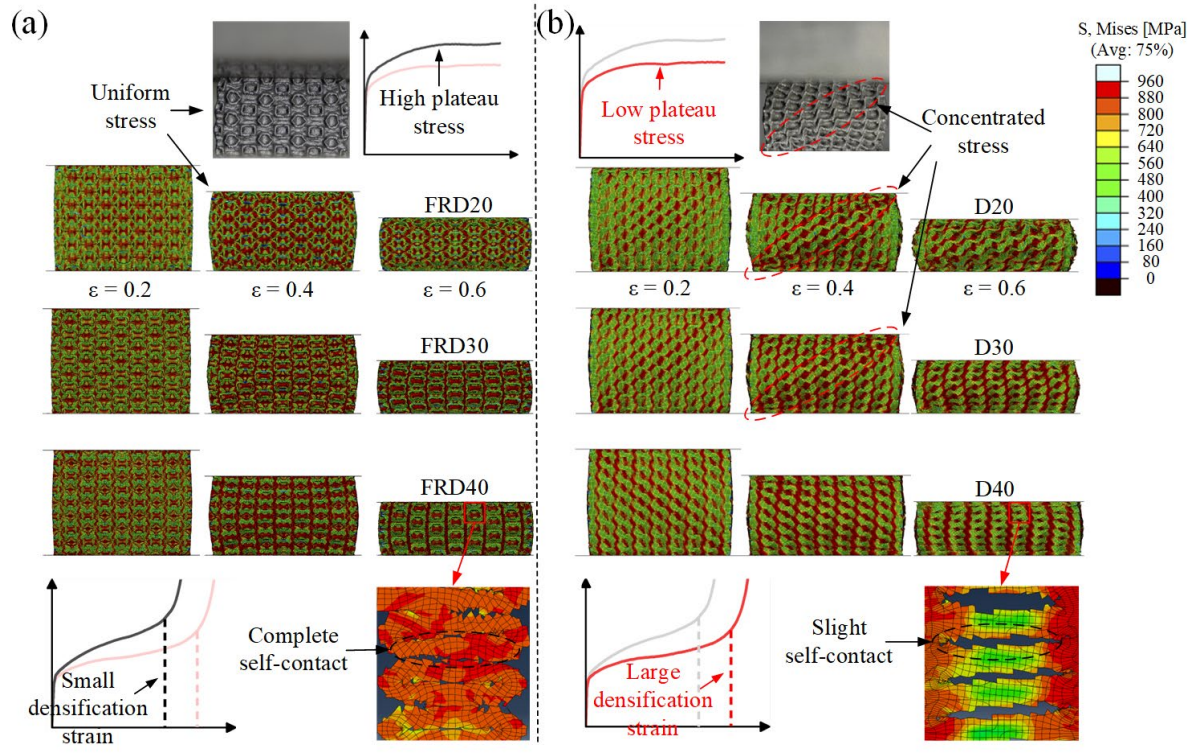

Fig. 17. von Mises stress contours of (a) F-RD and (b) D lattice structures with relative densities of 20%, 30%, and 40%. Numerical simulations predicted the deformation behavior and stress distribution. F-RD produced a more uniform stress distribution, resulting in higher plateau stress, and the later self-contact of the D structure resulted in a greater densification strain.

The work done in this study on numerical simulations could guide the design of TPMS structures, and the advantages in mechanical performance make them attractive for the application in protective devices and energy absorbers. For example, bending-dominated deformation of TPMS structures is expected in the design of helmets [62], providing a smooth and extensive plateau stress and avoiding the damage caused by instantaneous peak stresses. Moreover, for critical energy-absorbing components in the automobile [63] and aerospace industries [64], such as energy-absorbing boxes [65] and shock absorbers [66], the F-RD structure could satisfy both energy absorption and lightweight requirements.

5. Concluding remarks

The present study systematically investigated the mechanical properties of eight TPMS lattice structures under quasi-static compression. Based on the experimental data, five meshing strategies were compared for the P, G, and F-K lattice structures in terms of modeling ease, computational efficiency, data management, and simulation accuracy.

It was found that the lattice structures in this study exhibited homogenous deformation mode during the compression process and no cracks were observed. According to the G-A model, all lattice structures exhibited a bending-dominated deformation mode. The homogenous deformation pattern for different TPMS structures led to a more uniform stress distribution and more efficient mechanical properties. Furthermore, the energy absorption of the TPMS lattice was quantified by the G-A model. The F-RD lattice structures absorbed more energy at relative densities less than 30%, and the D lattice structures did at relative densities greater than 30%.

The numerical study found that among the five meshing strategies, the quadrilateral element shell models showed satisfactory results in computational efficiency for lattice structures with a low relative density or thin wall thickness. On the contrary, the voxel model showed the best results for lattice structures with a high relative density or thicker wall thickness in terms of both modeling ease, computational efficiency, and accuracy. Finally, from the simulation for F-RD and D structures using the voxel model, the F-RD had a more uniform stress distribution and could produce better loading-bearing capacity in the plateau region, while the D had a later onset of internal wall self-contact, leading to a larger densification strain. These results help to analyze the energy absorption mechanism of the TPMS lattices.

The current work is still inadequate, and the following topics may be considered for future research. Firstly, the 3D DIC may be applied to better analyze the deformation mechanism of the structures [67]. Secondly, more factors should be considered comprehensively in the numerical study, such as time steps and the number of integration points in the elements. Finally, the TPMS structure can be further optimized for better mechanical performance [68, 69]. For example, the mechanical properties can be enhanced

by parametric optimization [70-73] and topology optimization [74]. In addition, multiobjective optimization can be performed to consider conflicting objectives (e.g., light weight and energy absorption) [75-78]. Furthermore, another focus of recent research interest is the optimization of structural performance using efficient and robust machine learning techniques [13, 79, 80].

Acknowledgment

This work was supported by The National Natural Science Foundation of China (52165029 and 51805123， Key Program 52231012), Hainan Key Research and Development program (ZDYF2021GXJS022). The last author is a recipient of the ARC Discovery Early Career Research Award (DE210101676).

References

[1] T.J. Lu, H.A. Stone, M.F. Ashby, Heat transfer in open-cell metal foams, Acta Materialia 46(10) (1998) 3619-3635.

[2] K. Boomsma, D. Poulikakos, F. Zwick, Metal foams as compact high performance heat exchangers, Mechanics of Materials 35(12) (2003) 1161-1176.

[3] A. Montillet, J. Comiti, J. Legrand, Application of metallic foams in electrochemical reactors of the filter-press type: Part II Mass transfer performance, Journal of Applied Electrochemistry 24(5) (1994) 384-389.

[4] J. Liu, T. Chen, Y. Zhang, G. Wen, Q. Qing, H. Wang, R. Sedaghati, Y.M. Xie, On sound insulation of pyramidal lattice sandwich structure, Composite Structures 208 (2019) 385-394.

[5] R.A.W. Mines, S. Tsopanos, Y. Shen, R. Hasan, S.T. McKown, Drop weight impact behaviour of sandwich panels with metallic micro lattice cores, International Journal of Impact Engineering 60 (2013) 120-132.

[6] X. Xu, Y. Zhang, X. Wang, J. Fang, J. Chen, J. Li, Searching superior crashworthiness performance by constructing variable thickness honeycombs with biomimetic cells, International Journal of Mechanical Sciences 235 (2022) 107718.

[7] N. Qiu, J. Zhang, F. Yuan, Z. Jin, Y. Zhang, J. Fang, Mechanical performance of triply periodic minimal surface structures with a novel hybrid gradient fabricated by selective laser melting, Engineering Structures 263 (2022) 114377.

[8] M. Zhao, D.Z. Zhang, F. Liu, Z. Li, Z. Ma, Z. Ren, Mechanical and energy absorption characteristics of additively manufactured functionally graded sheet lattice structures with minimal surfaces, International Journal of Mechanical Sciences 167 (2020) 105262.

[9] D.-J. Yoo, Recent trends and challenges in computer-aided design of additive manufacturing-based biomimetic scaffolds and bioartificial organs, International Journal of Precision Engineering and Manufacturing 15(10) (2014) 2205-2217.

[10] D.-J. Yoo, New paradigms in cellular material design and fabrication, International Journal of Precision Engineering and Manufacturing 16(12) (2015) 2577-2589.

[11] O. Al-Ketan, R. Rowshan, R.K. Abu Al-Rub, Topology-mechanical property relationship of 3D printed strut, skeletal, and sheet based periodic metallic cellular materials, Additive Manufacturing 19 (2018) 167-183.
[12] M. Jin, Q. Feng, X. Fan, Z. Luo, Q. Tang, J. Song, S. Ma, Y. Nie, P. Jin, M. Zhao, Investigation on the mechanical properties of TPMS porous structures fabricated by laser powder bed fusion, Journal of Manufacturing Processes 76 (2022) 559-574.
[13] Y. Wu, J. Fang, C. Wu, C. Li, G. Sun, Q. Li, Additively manufactured materials and structures: A state-of-the-art review on their mechanical characteristics and energy absorption, International Journal of Mechanical Sciences 246 (2023) 108102.
[14] N. Guo, M.C. Leu, Additive manufacturing: technology, applications and research needs, Frontiers of Mechanical Engineering 8(3) (2013) 215-243.
[15] L.E. Murr, S.M. Gaytan, D.A. Ramirez, E. Martinez, J. Hernandez, K.N. Amato, P.W. Shindo, F.R. Medina, R.B. Wicker, Metal Fabrication by Additive Manufacturing Using Laser and Electron Beam Melting Technologies, Journal of Materials Science & Technology 28(1) (2012) 1-14.
[16] X. Tan, Y. Kok, Y.J. Tan, M. Descoins, D. Mangelinck, S.B. Tor, K.F. Leong, C.K. Chua, Graded microstructure and mechanical properties of additive manufactured Ti–6Al–4V via electron beam melting, Acta Materialia 97 (2015) 1-16.
[17] D. Herzog, V. Seyda, E. Wycisk, C. Emmelmann, Additive manufacturing of metals, Acta Materialia 117 (2016) 371-392.
[18] C.Y. Yap, C.K. Chua, Z.L. Dong, Z.H. Liu, D.Q. Zhang, L.E. Loh, S.L. Sing, Review of selective laser melting: Materials and applications, Applied Physics Reviews 2(4) (2015) 041101.
[19] N. Qiu, J. Zhang, C. Li, Y. Shen, J. Fang, Mechanical properties of three-dimensional functionally graded triply periodic minimum surface structures, International Journal of Mechanical Sciences 246 (2023) 108118.
[20] J. Zhang, Y. Liu, B.B. Babamiri, Y. Zhou, M. Dargusch, K. Hazeli, M.-X. Zhang, Enhancing specific energy absorption of additively manufactured titanium lattice structures through simultaneous manipulation of architecture and constituent material, Additive Manufacturing 55 (2022) 102887.
[21] L. Yang, M. Ferrucci, R. Mertens, W. Dewulf, C. Yan, Y. Shi, S. Yang, An investigation into the effect of gradients on the manufacturing fidelity of triply periodic minimal surface structures with graded density fabricated by selective laser melting, Journal of Materials Processing Technology 275 (2020) 116367.
[22] G. Wang, L. Shen, J. Zhao, H. Liang, D. Xie, Z. Tian, C. Wang, Design and Compressive Behavior of Controllable Irregular Porous Scaffolds: Based on Voronoi-Tessellation and for Additive Manufacturing, ACS Biomater Sci Eng 4(2) (2018) 719-727.
[23] D.W. Abueidda, M. Bakir, R.K. Abu Al-Rub, J.S. Bergström, N.A. Sobh, I. Jasiuk, Mechanical properties of 3D printed polymeric cellular materials with triply periodic minimal surface architectures, Materials & Design 122 (2017) 255-267.
[24] S.N. Khaderi, V.S. Deshpande, N.A. Fleck, The stiffness and strength of the gyroid lattice, International Journal of Solids and Structures 51(23-24) (2014) 3866-3877.
[25] D.W. Abueidda, R.K. Abu Al-Rub, A.S. Dalaq, D.-W. Lee, K.A. Khan, I. Jasiuk, Effective conductivities and elastic moduli of novel foams with triply periodic minimal surfaces, Mechanics of Materials 95 (2016) 102-115.
[26] B.D. Nguyen, J.S. Cho, K. Kang, Optimal design of “Shellular”, a micro-architectured material with ultralow density, Materials & Design 95 (2016) 490-500.
[27] X. Fan, Q. Tang, Q. Feng, S. Ma, J. Song, M. Jin, F. Guo, P. Jin, Design, mechanical properties and

energy absorption capability of graded-thickness triply periodic minimal surface structures fabricated by selective laser melting, International Journal of Mechanical Sciences 204 (2021) 106586.
[28] L. Zhang, S. Feih, S. Daynes, S. Chang, M.Y. Wang, J. Wei, W.F. Lu, Energy absorption characteristics of metallic triply periodic minimal surface sheet structures under compressive loading, Additive Manufacturing 23 (2018) 505-515.
[29] S. AlMahri, R. Santiago, D.-W. Lee, H. Ramos, H. Alabdouli, M. Alteneiji, Z. Guan, W. Cantwell, M. Alves, Evaluation of the dynamic response of triply periodic minimal surfaces subjected to high strain-rate compression, Additive Manufacturing 46 (2021) 102220.
[30] H. Yin, Z. Liu, J. Dai, G. Wen, C. Zhang, Crushing behavior and optimization of sheet-based 3D periodic cellular structures, Composites Part B: Engineering 182 (2020) 107565.
[31] N. Baghous, I. Barsoum, R.K. Abu Al-Rub, Generalized yield surface for sheet-based triply periodic minimal surface lattices, International Journal of Mechanical Sciences 252 (2023) 108370.
[32] M. Afshar, A. Pourkamali Anaraki, H. Montazerian, Compressive characteristics of radially graded porosity scaffolds architectured with minimal surfaces, Mater Sci Eng C Mater Biol Appl 92 (2018) 254-267.
[33] Y. Wang, F. Liu, X. Zhang, K. Zhang, X. Wang, D. Gan, B. Yang, Cell-size graded sandwich enhances additive manufacturing fidelity and energy absorption, International Journal of Mechanical Sciences 211 (2021) 106798.
[34] N. Kladovasilakis, K. Tsongas, D. Tzetzis, Mechanical and FEA-Assisted Characterization of Fused Filament Fabricated Triply Periodic Minimal Surface Structures, Journal of Composites Science 5(2) (2021) 58.
[35] F. Ren, C. Zhang, W. Liao, T. Liu, D. Li, X. Shi, W. Jiang, C. Wang, J. Qi, Y. Chen, Z. Wang, Transition boundaries and stiffness optimal design for multi-TPMS lattices, Materials & Design 210 (2021) 110062.
[36] D. Li, W. Liao, N. Dai, Y.M. Xie, Comparison of Mechanical Properties and Energy Absorption of Sheet-Based and Strut-Based Gyroid Cellular Structures with Graded Densities, Materials 12(13) (2019) 2183.
[37] L. Yang, C. Yan, W. Cao, Z. Liu, B. Song, S. Wen, C. Zhang, Y. Shi, S. Yang, Compression–compression fatigue behaviour of gyroid-type triply periodic minimal surface porous structures fabricated by selective laser melting, Acta Materialia 181 (2019) 49-66.
[38] B. Zhang, R. Yao, J. Fang, R. Ma, T. Pang, D. Zhou, Energy absorption behaviors and optimization design of thin-walled double-hat beam under bending, Thin-Walled Structures 179 (2022) 109577.
[39] X. Shi, W. Liao, P. Li, C. Zhang, T. Liu, C. Wang, J. Wu, Comparison of Compression Performance and Energy Absorption of Lattice Structures Fabricated by Selective Laser Melting, Advanced Engineering Materials 22(11) (2020) 2000453.
[40] X. Xu, Y. Zhang, J. Fang, X. Chen, Z. Liu, Y. Xu, Y. Gao, Axial mechanical properties and robust optimization of foam-filled hierarchical structures, Composite Structures 289 (2022) 115501.
[41] H. Jia, H. Lei, P. Wang, J. Meng, C. Li, H. Zhou, X. Zhang, D. Fang, An experimental and numerical investigation of compressive response of designed Schwarz Primitive triply periodic minimal surface with non-uniform shell thickness, Extreme Mechanics Letters 37 (2020) 100671.
[42] Y. Wang, X. Ren, Z. Chen, Y. Jiang, X. Cao, S. Fang, T. Zhao, Y. Li, D. Fang, Numerical and experimental studies on compressive behavior of Gyroid lattice cylindrical shells, Materials & Design 186 (2020) 108340.
[43] I. Maskery, L. Sturm, A.O. Aremu, A. Panesar, C.B. Williams, C.J. Tuck, R.D. Wildman, I.A. Ashcroft, R.J.M. Hague, Insights into the mechanical properties of several triply periodic minimal surface lattice

structures made by polymer additive manufacturing, Polymer 152 (2018) 62-71.
[44] U. Simsek, A. Akbulut, C.E. Gayir, C. Basaran, P. Sendur, Modal characterization of additively manufactured TPMS structures: comparison between different modeling methods, The International Journal of Advanced Manufacturing Technology 115(3) (2020) 657-674.
[45] D.J. Yoo, Porous scaffold design using the distance field and triply periodic minimal surface models, Biomaterials 32(31) (2011) 7741-7754.
[46] A.M. Abou-Ali, O. Al-Ketan, D.-W. Lee, R. Rowshan, R.K. Abu Al-Rub, Mechanical behavior of polymeric selective laser sintered ligament and sheet based lattices of triply periodic minimal surface architectures, Materials & Design 196 (2020) 109100.
[47] N. Novak, O. Al-Ketan, L. Krstulović-Opara, R. Rowshan, R.K. Abu Al-Rub, M. Vesenjak, Z. Ren, Quasi-static and dynamic compressive behaviour of sheet TPMS cellular structures, Composite Structures 266 (2021) 113801.
[48] O. Al-Ketan, R. Rowshan, A.N. Palazotto, R.K. Abu Al-Rub, On Mechanical Properties of Cellular Steel Solids With Shell-Like Periodic Architectures Fabricated by Selective Laser Sintering, Journal of Engineering Materials and Technology 141(2) (2019) 021009.
[49] B.B. Ravichander, S.H. Jagdale, A. Jabed, G. Kumar, Mechanical and corrosion behavior of sheet-based 316L TPMS structures, International Journal of Mechanical Sciences 254 (2023) 108439.
[50] J. Fu, J. Ding, S. Qu, L. Zhang, M.Y. Wang, M.W. Fu, X. Song, Improved light-weighting potential of SS316L triply periodic minimal surface shell lattices by micro laser powder bed fusion, Materials & Design 222 (2022) 111018.
[51] M. Rezapourian, I. Jasiuk, M. Saarna, I. Hussainova, Selective laser melted Ti6Al4V split-P TPMS lattices for bone tissue engineering, International Journal of Mechanical Sciences 251 (2023) 108353.
[52] L. Yang, R. Mertens, M. Ferrucci, C. Yan, Y. Shi, S. Yang, Continuous graded Gyroid cellular structures fabricated by selective laser melting: Design, manufacturing and mechanical properties, Materials & Design 162 (2019) 394-404.
[53] H. Zhou, M. Zhao, Z. Ma, D.Z. Zhang, G. Fu, Sheet and network based functionally graded lattice structures manufactured by selective laser melting: Design, mechanical properties, and simulation, International Journal of Mechanical Sciences 175 (2020) 105480.
[54] J. Fang, G. Sun, N. Qiu, N.H. Kim, Q. Li, On design optimization for structural crashworthiness and its state of the art, Structural and Multidisciplinary Optimization 55(3) (2016) 1091-1119.
[55] I. Maskery, N.T. Aboulkhair, A.O. Aremu, C.J. Tuck, I.A. Ashcroft, R.D. Wildman, R.J.M. Hague, A mechanical property evaluation of graded density Al-Si10-Mg lattice structures manufactured by selective laser melting, Materials Science and Engineering: A 670 (2016) 264-274.
[56] X. Guo, J. Ding, X. Li, S. Qu, X. Song, J.Y.H. Fuh, W.F. Lu, W. Zhai, Enhancement in the mechanical behaviour of a Schwarz Primitive periodic minimal surface lattice structure design, International Journal of Mechanical Sciences 216 (2022) 106977.
[57] J. Plocher, A. Panesar, Effect of density and unit cell size grading on the stiffness and energy absorption of short fibre-reinforced functionally graded lattice structures, Additive Manufacturing 33 (2020) 101171.
[58] V.S. Deshpande, M.F. Ashby, N.A. Fleck, Foam topology: bending versus stretching dominated architectures, Acta Materialia 49(6) (2001) 1035-1040.
[59] C. Li, J. Fang, Y. Wan, N. Qiu, G. Steven, Q. Li, Phase field fracture model for additively manufactured metallic materials, International Journal of Mechanical Sciences 251 (2023) 108324.
[60] A.O. Aremu, J.P.J. Brennan-Craddock, A. Panesar, I.A. Ashcroft, R.J.M. Hague, R.D. Wildman, C. Tuck,

A voxel-based method of constructing and skinning conformal and functionally graded lattice structures suitable for additive manufacturing, Additive Manufacturing 13 (2017) 1-13.
[61] S. Abaqus, A. Fallis, D. Techniques, ABAQUS analysis user's guide (6.14), Dassault Systemes Simulia Corp., Providence (2014).
[62] R. Adams, S. Townsend, S. Soe, P. Theobald, Finite element-based optimisation of an elastomeric honeycomb for impact mitigation in helmet liners, International Journal of Mechanical Sciences 214 (2022) 106920.
[63] S. Soni, S.K. Pradhan, Improving crash worthiness and dynamic performance of frontal plastic automotive body components, Materials Today: Proceedings 27 (2020) 2308-2313.
[64] L. An, X. Wu, K. Wang, R. Li, Z. Li, G. Li, Crack modes and toughening strategies of bioinspired 3D printed double-helicoidal architectures, International Journal of Mechanical Sciences 253 (2023) 108388.
[65] W. Hou, P. He, Y. Yang, L. Sang, Crashworthiness optimization of crash box with 3D-printed lattice structures, International Journal of Mechanical Sciences 247 (2023) 108198.
[66] P. Sonowal, K.M. Pandey, K.K. Sharma, Design and static analysis of landing gear shock absorber of commercial aircraft, Materials Today: Proceedings 45 (2021) 6712-6717.
[67] M. Ye, J. Liang, L. Li, Y. Zong, J. Guo, Z. Tang, S. Ma, R. Chen, Simultaneous measurement of external and internal surface shape and deformation based on photogrammetry and stereo-DIC, Optics and Lasers in Engineering 158 (2022) 107179.
[68] B. Hu, Z. Wang, C. Du, W. Zou, W. Wu, J. Tang, J. Ai, H. Zhou, R. Chen, B. Shan, Multiobjective Bayesian optimization accelerated design of TPMS structures, International Journal of Mechanical Sciences 244 (2023) 108085.
[69] M. Zhao, X. Li, D.Z. Zhang, W. Zhai, TPMS-based interpenetrating lattice structures: Design, mechanical properties and multiscale optimization, International Journal of Mechanical Sciences 244 (2023) 108092.
[70] J. Fang, Y. Gao, G. Sun, G. Zheng, Q. Li, Dynamic crashing behavior of new extrudable multi-cell tubes with a functionally graded thickness, International Journal of Mechanical Sciences 103 (2015) 63-73.
[71] G. Sun, T. Pang, J. Fang, G. Li, Q. Li, Parameterization of criss-cross configurations for multiobjective crashworthiness optimization, International Journal of Mechanical Sciences 124-125 (2017) 145-157.
[72] D.K. Pokkalla, L.H. Poh, S.T. Quek, Isogeometric shape optimization of missing rib auxetics with prescribed negative Poisson's ratio over large strains using genetic algorithm, International Journal of Mechanical Sciences 193 (2021) 106169.
[73] D.K. Pokkalla, Z.-P. Wang, L.H. Poh, S.T. Quek, Isogeometric shape optimization of smoothed petal auxetics with prescribed nonlinear deformation, Computer Methods in Applied Mechanics and Engineering 356 (2019) 16-43.
[74] N. Qiu, Y. Gao, J. Fang, G. Sun, N.H. Kim, Topological design of multi-cell hexagonal tubes under axial and lateral loading cases using a modified particle swarm algorithm, Applied Mathematical Modelling 53 (2018) 567-583.
[75] N. Qiu, Y. Gao, J. Fang, G. Sun, Q. Li, N.H. Kim, Crashworthiness optimization with uncertainty from surrogate model and numerical error, Thin-Walled Structures 129 (2018) 457-472.
[76] F.V. Senhora, E.D. Sanders, G.H. Paulino, Optimally-Tailored Spinodal Architected Materials for Multiscale Design and Manufacturing, Advanced Materials 34(26) (2022) 2109304.
[77] N. Qiu, Y. Gao, J. Fang, Z. Feng, G. Sun, Q. Li, Crashworthiness analysis and design of multi-cell hexagonal columns under multiple loading cases, Finite Elements in Analysis and Design 104 (2015) 89-101.

[78] N. Qiu, Y. Gao, J. Fang, Z. Feng, G. Sun, Q. Li, Theoretical prediction and optimization of multi-cell hexagonal tubes under axial crashing, Thin-Walled Structures 102 (2016) 111-121.
[79] S. Kumar, S. Tan, L. Zheng, D.M. Kochmann, Inverse-designed spinodoid metamaterials, npj Computational Materials 6(1) (2020) 73.
[80] X. Zheng, X. Zhang, T.-T. Chen, I. Watanabe, Deep Learning in Mechanical Metamaterials: From Prediction and Generation to Inverse Design, Advanced Materials n/a(n/a) (2023) 2302530.